Therapeutic and vaccine-induced cross-reactive antibodies with effector function against emerging Omicron variants

Amin Addetia[1,*], Luca Piccoli[2,*], James Brett Case[3,*], Young-Jun Park[1,*], Martina Beltramello[2], Barbara Guarino[2], Ha Dang[4], Dora Pinto[2], Suzanne M. Scheaffer[3], Kaitlin Sprouse[1], Jessica Bassi[2], Chiara Silacci-Fregni[2], Francesco Muoio[2], Marco Dini[2], Lucia Vincenzetti[2], Rima Acosta[4], Daisy Johnson[4], Sambhavi Subramanian[4], Christian Saliba[2], Martina Giurdanella[2], Gloria Lombardo[2], Giada Leoni[2], Katja Culap[2], Carley McAlister[4], Anushka Rajesh[4], Exequiel Dellota Jr.[4], Elisabetta Cameroni[2], Bradley Whitener[3], Olivier Giannini[5,6], Alessandro Ceschi[5,7,8,9], Paolo Ferrari[5,10,11], Alessandra Franzetti-Pellanda[12], Maira Biggiogero[12], Christian Garzoni[13], Stephanie Zappi[14], Luca Bernasconi[15], Min Jeong Kim[14], Gretja Schnell[4], Nadine Czudnochowski[4], Nicholas Franko[16], Jennifer K. Logue[16], Courtney Yoshiyama[1], Cameron Stewart[1], Helen Chu[16], Michael A. Schmid[2], Lisa A. Purcell[4], Gyorgy Snell[4], Antonio Lanzavecchia[2], Michael S. Diamond[3,17,18,19,20,#], Davide Corti[2,#], David Veesler[1,21,#]

[1]Department of Biochemistry, University of Washington, Seattle, WA 98195, USA.
[2]Humabs BioMed SA, a subsidiary of Vir Biotechnology, 6500 Bellinzona, Switzerland.
[3]Department of Medicine, Washington University School of Medicine, St. Louis, MO, USA.
[4]Vir Biotechnology, San Francisco, CA 94158, USA.
[5]Faculty of Biomedical Sciences, Università della Svizzera italiana, Lugano, Switzerland.
[6]Department of Medicine, Ente Ospedaliero Cantonale, Bellinzona, Switzerland
[7]Clinical Trial Unit, Ente Ospedaliero Cantonale, Lugano, Switzerland.
[8]Division of Clinical Pharmacology and Toxicology, Institute of Pharmacological Sciences of Southern Switzerland, Ente Ospedaliero Cantonale, Lugano, Switzerland.
[9]Department of Clinical Pharmacology and Toxicology, University Hospital Zurich, Zurich, Switzerland
[10]Division of Nephrology, Ente Ospedaliero Cantonale, Lugano, Switzerland.
[11]Clinical School, University of New South Wales, Sydney, New South Wales, Australia.
[12]Clinical Research Unit, Clinica Luganese Moncucco, Lugano, Switzerland
[13]Clinic of Internal Medicine and Infectious Diseases, Clinica Luganese Moncucco, Lugano, Switzerland
[14]Division of Nephrology, Cantonal Hospital Aarau, Aarau, Switzerland
[15]Institute of Laboratory Medicine, Cantonal Hospital Aarau, Aarau, Switzerland
[16]Division of Allergy and Infectious Diseases, University of Washington, Seattle, WA 98195, USA.
[17]Department of Pathology & Immunology, Washington University School of Medicine, St. Louis, MO, USA
[18]Department of Molecular Microbiology, Washington University School of Medicine, St. Louis, MO, USA
[19]Andrew M. and Jane M. Bursky Center for Human Immunology and Immunotherapy Programs, Washington University School of Medicine, Saint Louis, MO, USA.
[20]Center for Vaccines and Immunity to Microbial Pathogens, Washington University School of Medicine, Saint Louis, MO, USA.
[21]Howard Hughes Medical Institute, University of Washington, Seattle, WA 98195, USA.

*These authors contributed equally
[#]Correspondence: mdiamond@wustl.edu, dcorti@vir.bio, dveesler@uw.edu

Currently circulating SARS-CoV-2 variants acquired convergent mutations at receptor-binding domain (RBD) hot spots[1]. Their impact on viral infection, transmission, and efficacy of vaccines and therapeutics remains poorly understood. Here, we demonstrate that recently emerged BQ.1.1. and XBB.1 variants bind ACE2 with high affinity and promote membrane fusion more efficiently than earlier Omicron variants. Structures of the BQ.1.1 and XBB.1 RBDs bound to human ACE2 and S309 Fab (sotrovimab parent) explain the altered ACE2 recognition and preserved antibody binding through conformational selection. We show that sotrovimab binds avidly to all Omicron variants, promotes Fc-dependent effector functions and protects mice challenged with BQ.1.1, the variant displaying the greatest loss of neutralization. Moreover, in several donors vaccine-elicited plasma antibodies cross-react with and trigger effector functions against Omicron variants despite reduced neutralizing activity. Cross-reactive RBD-directed human memory B cells remained dominant even after two exposures to Omicron spikes, underscoring persistent immune imprinting. Our findings suggest that this previously overlooked class of cross-reactive antibodies, exemplified by S309, may contribute to protection against disease caused by emerging variants through elicitation of effector functions.

The emergence of the Omicron variant of concern at the end of 2021 marked a new phase of the COVID-19 pandemic[2]. Omicron lineages accumulated tens of amino acid mutations in their spike (S) glycoprotein that enhanced receptor engagement, altered the preferred internalization route in cells and promoted immune evasion from neutralizing antibodies of unprecedented magnitude[3–15]. As a result, most countries experienced repeated waves of infections in 2021 and 2022, driven by successive Omicron lineages (e.g., BA.1/BA.1.1, BA.2, BA.5), including in individuals who received multiple COVID-19 vaccine doses.

Currently, many different Omicron variant lineages are co-circulating worldwide. Due to convergent evolution, many of these lineages independently acquired identical or similar amino acid mutations at key antigenic sites in the RBD and in the NTD, relative to their presumed BA.2 and BA.5 ancestors[1]. The BA.2.75.2 lineage rose in frequency in multiple countries (e.g., India) and has the following RBD residue mutations relative to BA.2: D339H, R346T, G446S, N460K, F486S and R493Q. XBB.1 is an inter-Omicron recombinant lineage, derived from BJ.1 and BA.2.75, and harbors the following RBD residue mutations relative to BA.2: D339H, R346T, L368I, V445P, G446S, N460K, F486S, F490S, R493Q **(Fig. 1a)**. Furthermore, the XBB.1.5 lineage, which contains a proline at position 486 instead of a serine (F486 in Wuhan), is currently rising in the US with ~43% of cases attributed to the variant as of 14 January 2023. BQ.1 and BQ.1.1 are dominant in several Western countries and account for 56% of all sequenced SARS-CoV-2 genomes in the US (https://covid.cdc.gov/covid-data-tracker/#variant-proportions). BQ1.1 has the following residue mutations relative to BA.5: R346T, K444T and N460K **(Fig. 1a)**. Several of the mutated amino acid positions present in the XBB.1(.5) and BQ.1.1 variant S glycoproteins were previously detected in cryptic lineages through wastewater sequencing[16] and virtually all of them map to key NTD and RBD antigenic sites.

SARS-CoV-2 S recognizes angiotensin-converting enzyme 2 (ACE2) as its main entry receptor, leading to membrane fusion and viral entry[17–20]. RBD-directed antibodies account for most neutralizing activity against vaccine-matched and vaccine-mismatched viruses, whereas the N-terminal domain is mostly targeted by variant-specific neutralizing antibodies[21–34]. Here, we set out to understand how the constellation of mutations in the BQ.1.1, XBB.1(.5) and BA.2.75.2 S variants affect the functional properties of SARS-CoV-2, humoral and memory immunity in humans, and recognition by therapeutic antibodies.

Functional properties of BQ.1.1, XBB.1 and BA.2.75.2 S

We first determined the binding kinetics and affinity of the monomeric human ACE2 ectodomain to immobilized variant RBDs using biolayer interferometry **(Fig. 1b, Extended Data Fig. 1** and **Supplementary Table 1)**. We measured identical equilibrium dissociation constants for the BQ.1.1 and BA.5 RBDs (K_D= 12.8 nM and 13.7 nM, respectively), indicating that the additional BQ.1.1 mutations, which map outside the ACE2-binding interface, do not influence receptor engagement **(Fig. 1b, Extended Data Fig. 1** and **Supplementary Table 1)**. The enhanced ACE2 binding affinity of the BA.2.75.2 RBD (K_D= 26.2 nM), relative to BA.2, results from the R493Q reversion, as G446S has a negligible effect and F486S has a deleterious effect on ACE2 engagement based on mutagenesis and deep-mutational scanning data[35]. We also determined that ACE2 bound to the XBB.1 RBD with an affinity comparable to the Wuhan-Hu-1 (Wu) RBD (K_D= 88.4 nM and K_D= 101.1 nM, respectively). As V445P does not change the conformation of the ACE2-bound XBB.1 RBD, relative to BQ.1.1, and none of the three residue substitutions compared to BA.2.75.2 involve side chain-mediated contacts with the host receptor, it is possible that the V445P mutation alters the backbone conformational dynamic of the free XBB.1 RBD and dampens ACE2 binding. We observed a similar ranking of these variant RBDs using surface plasmon resonance (SPR) to determine ACE2 binding affinities **(Fig. 1c, Extended Data Fig. 1** and **Supplementary Table 2)**. Modulation of ACE2 binding resulted from off-rate differences, whereas on-rates remained comparable across all variants tested, in agreement with observations made with previous variants[3,5,35–37]. Collectively these data indicate that BQ.1.1, BA.2.75.2 and BA.5 have comparably high ACE2 binding affinity, suggesting that the BQ.1.1 and BA.2.75.2 viral fitness is not limited by this step of host cell invasion, whereas the lower ACE2-binding affinity of XBB.1 might have limited its spread.

We next compared the kinetics and magnitude of cell-cell fusion promoted by the Wu-G614, Delta, BA.1, BA.2, BA.5, BQ.1.1, BA.2.75.2 and XBB.1 S glycoproteins. This live cell imaging assay uses a split green fluorescent protein (GFP) system with VeroE6 target cells stably expressing TMPRSS2 and GFP $\beta_{1\text{-}10}$ strands and BHK-21 effector cells stably expressing GFP β_{11} strand and transiently transfected with S[3,38]. We observed slower and reduced fusogenicity for the BA.5, BA.2 and BA.1 S glycoproteins compared with Wu-G614 and even more so relative to Delta S[12] **(Fig. 1d** and **Extended Data Fig. 2)**, in line with previous findings and the lack of syncytia formation observed with authentic viruses[3,7]. BQ.1.1, BA.2.75.2 and XBB.1 S, however, promoted membrane fusion more efficiently than the earlier Omicron variants **(Fig. 1d** and **Extended Data Fig. 2)**, suggesting enhanced fusogenic potential of these recently emerged variants.

We and others previously showed that BA.1, BA.2 and BA.5 had an altered cell entry pathway relative to previous SARS-CoV-2 strains, with Omicron variants entering preferentially

through the endosomal entry route (cathepsin-mediated) as opposed to plasma membrane fusion (TMPRSS2-mediated)[6–8,19,39]. To assess the preferred cell entry route of the emerging Omicron variants, we investigated the impact of protease inhibitors on entry of non-replicative vesicular stomatitis virus (VSV) pseudotyped with S glycoproteins into VeroE6-TMPRSS2 cells (enabling both plasma membrane and endosomal entry routes) and HEK293T-ACE2 cells (enabling endosomal entry only). The serine protease (TMPRSS2) inhibitors camostat and nafamostat potently blocked entry of Wu-G614 and Delta S VSV pseudoviruses in VeroE6-TMPRSS2 cells, but had limited effect on any of the Omicron variants, including BQ.1.1, BA.2.75.2 and XBB.1 **(Fig. 1e)**. Reciprocally, the cathepsin B and L inhibitor E64d more significantly inhibited the entry of BA.1, BA.2 and BA.5 S VSV pseudoviruses relative to Wu-G614, whereas no significant difference in entry was measured for Delta, BA.2.75.2, BQ.1.1 or XBB.1 S VSV compared to Wu-G614 in VeroE6-TMPRSS2 cells (**Fig. 1e**). Furthermore, BQ.1.1 and XBB.1 S-mediated entry was also less affected by E-64d than all other variant S evaluated in HEK293T-ACE2 cells **(Fig. 1f** and **Extended Data Fig. 2)**. These findings indicate a possible alteration of protease requirements for BQ.1.1 and XBB.1 S-mediated entry, relative to other Omicron lineages assessed. The inefficient use of TMPRSS2 observed, however, concurs with the identical BQ.1.1, BA.2.75.2 and XBB.1 S_2 subunit sequences, particularly the presence of the N969K substitution, which was previously identified as the key change accounting for the switch from plasma membrane to endosomal cell entry routes of Omicron variants[6–8].

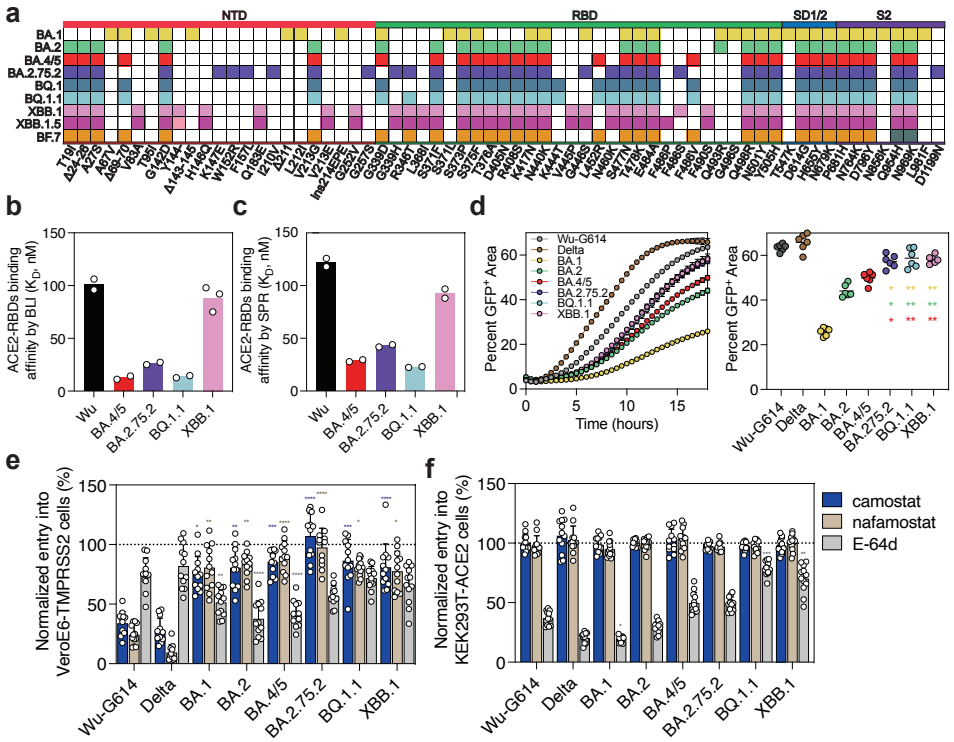

Fig. 1. Functional properties of the newly emerged BQ.1.1, XBB.1 and BA.2.75.2 variant S glycoproteins. a, Schematic view of S mutations carried by SARS-CoV-2 variants used in this study. **b, c,** Equilibrium dissociation constants (K_D) measured by biolayer interferometry (b) and surface plasmon resonance (c) for binding of the monomeric human ACE2 ectodomain to the

immobilized Wu, BA.4/5, BA.2.75.2, BQ.1.1, or XBB.1 RBDs. **d,** Cell-cell fusion (expressed as the percentage of GFP^+ area) between cells expressing the Wu-G614, Delta, BA.1, BA.2, BA.4/5, BA.2.75.2, BQ.1.1, or XBB.1 S glycoproteins and VeroE6-TMPRSS2 cells measured over an 18-hour time course experiment using a split GFP system (left panel). The mean magnitude of cell-cell fusion at 18 hours is shown on the right panel. Data are from 6 fields of view from a single experiment and representative of results from two independent biological replicates. Comparisons of fusogenicity mediated by BA.1, BA.2, or BA.4/5 S to BA.2.75.2, BQ.1.1, or and XBB.1 S were completed using the Dunnett's test with the colors of the asterisks indicating which group the comparison is done with (BA.1: gold; BA.2: green; BA.4/5: red). **P < 0.01. **e, f,** Relative entry of VSV pseudotyped with the Wu-G614, Delta, BA.1, BA.2, BA.4/5, BA.2.75.2, BQ.1.1, or XBB.1 S in VeroE6-TMPRSS2 (e) or HEK293T-ACE2 (f) cells treated with 50 µM of camostat, nafamostat, or E-64d. Normalized entry was calculated based on entry values obtained for VeroE6-TMPRSS2 or HEK293T-ACE2 cells treated with DMSO only for each pseudovirus. Mean normalized entry and standard deviation are presented for each pseudovirus. Twelve technical replicates were performed for each pseudovirus and inhibitor and one experiment representative of two independent biological replicates is shown. Comparison of relative entry values were made between Wu-G614 S VSV pseudovirus and each of the examined SARS-CoV-2 variant S VSV pseudoviruses using the Dunnett's test. *P < 0.05; **P < 0.01; ***P < 0.001; ****P < 0.0001.

Structural analysis of the impact of BQ.1.1, XBB.1 and BA.2.75.2 RBD mutations on recognition by ACE2 and therapeutic antibodies

To reveal how amino acid substitutions in the BQ.1.1 and XBB.1 RBDs alter receptor recognition and key antigenic sites, we determined cryo-electron microscopy (cryoEM) structures of each RBD bound to the human ACE2 ectodomain and to the Fab fragment of the S309 monoclonal antibody (sotrovimab parent) **(Fig. 2a-b, Extended Data Fig. 3a-e** and **Supplementary Table 3)**. In both structures, the R493Q reversion likely relieves repulsion with ACE2 residue K31 and restores a network of local interactions similar to that made with the Wu RBD[40] **(Fig. 2c)**. Regarding interactions with therapeutic antibodies, the BQ.1.1 RBD structure shows that the K444T substitution would abrogate salt bridges with the carboxyl side chains of the LY-CoV1404 (bebtelovimab parent) and heavy chain residues D56 and D58 or of the COV2-2130 (cilgavimab parent) heavy chain residue D107 **(Fig 2d, e)**. Moreover, R346T (BQ.1.1/XBB.1) would abrogate a salt bridge with the COV2-2130 heavy chain residue D56; G446S (XBB.1) is expected to reduce COV2-2130 binding sterically and V445P (XBB.1) is expected to reduce binding due to a loss of van der Waals interactions with LY-CoV1404 **(Extended Data Fig. 3f)**. These data explain the decreased LY-CoV1404 binding observed by deep-mutational scanning of yeast-displayed mutant RBDs and the markedly reduced neutralization of LY-CoV1404, COV2-2130 or the COV2-2130/COV2-2196 (Evusheld parent) cocktail against the BQ.1.1 and XBB.1 variants[1,35,41].

The structures demonstrate that S309 binds to both the BQ.1.1 and XBB.1 RBDs and reveal the molecular basis for accommodation of the H339 residue in the XBB.1 epitope **(Fig. 2f)**. The S309 binding pose is indistinguishable from that observed when bound to the Wu RBD[42] or to the BA.1 RBD **(Fig. 2f)**. We recently described that the S371F mutation, which is present in BA.2, BA.5, BQ.1.1, XBB.1 and BA.2.75.2, leads to conformational changes of the RBD helix comprising residues 364-372 that are sterically incompatible with the glycan N343 conformation

observed in S309-bound spike structures[43]. In the BQ.1.1 structure, helix 364-372 is weakly resolved in the cryoEM map and adopts a conformation similar to that observed in the S309-bound BA.1 structure but distinct from apo BA.2[44] or apo BA.5 S[45] structures **(Fig. 2f)**. Residues 368-373 are disordered in the XBB.1 RBD cryoEM map, as is the case for the adjacent residues 380-392 **(Fig. 2f)**. These findings are strongly indicative of conformational frustration of helix 364-372 which is constrained to adopt an energetically disfavored conformation upon S309 binding and could explain the reduced neutralizing activity of this antibody against these variants[1,14,41,46,47] (**Fig. 3a**).

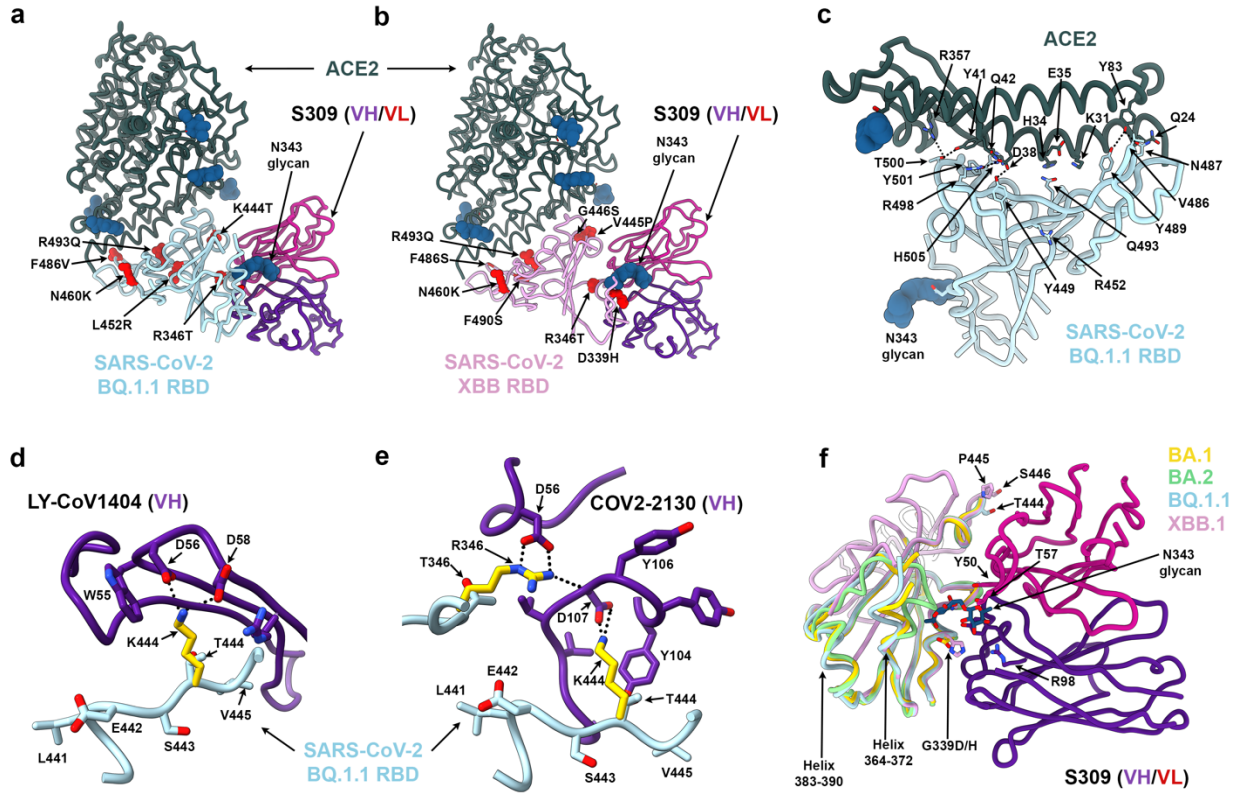

Fig. 2. Structural analysis of the BQ.1.1 and XBB.1 RBDs. a, b, CryoEM structures of the BQ.1.1 RBD (a, cyan) or the XBB.1 RBD (b, pink) bound to the human ACE2 ectodomain (green) and the S309 Fab fragment (purple/magenta for the heavy/light chains). Amino acid residues mutated relative to Omicron BA.2 are shown as red spheres. **c,** Zoomed-in view of the BQ.1.1 RBD interactions formed with human ACE2 with select amino acid residue side chains shown as sticks. N-linked glycans are shown as dark blue spheres in (a-c). **d, e,** Superimposition of the LY-CoV1404-bound Wu RBD structure (d, purple, PDB 7MMO) or of the COV2-2130-bound Wu RBD structure (e, purple, PDB 7L7E) onto the BQ.1.1 RBD cryoEM structure presented here highlighting the expected disruptions of electrostatic interactions with the monoclonal antibodies resulting from the K444T and the R346T RBD mutations. **f,** RBD-based superimpositions of the S309-bound BA.1 S (gold, PDB 7TLY), apo BA.2 S (green, PDB 7UB0), S309- and ACE2-bound BQ.1.1 (cyan) and XBB.1 (pink) RBD cryoEM structures (this study). S309 is rendered purple and magenta for heavy and light chains, respectively, and the N343 glycan along with select side chains are rendered as sticks. The expected N343 glycan clashes with BA.2 residues N370 and F371 (sticks) are indicated with a red/orange star.

220
221 **S309 activates effector functions and protects mice against BQ.1.1 challenge**
222 Based on the cryoEM visualization of S309 binding to the BQ.1.1 and XBB.1 RBDs, we
223 investigated the binding kinetics and affinity of the S309 Fab to the immobilized Wu, BA.1, BA.2
224 BA.2.75.2, BQ.1, BQ.1.1 and XBB.1 RBDs using SPR **(Fig. 3b)**. The binding affinity (K_D) of S309
225 against these variants decreased up to ~100 fold, primarily as a result of a slower association rate
226 as compared to that against Wu RBD. Little to no dissociation could be observed within the
227 timeframe of our experiment with any RBD evaluated (**Extended Data Fig. 4**). Structural
228 frustration of the RBD helix 364-372, in F371-harboring SARS-CoV-2 Omicron variants, combined
229 with substitutions at position 339 (G339D/H) likely modulate the observed on-rates through S309-
230 mediated backbone conformational and amino acid side chain rotameric selection. We also
231 observed that the sotrovimab IgG (derivative of S309) efficiently cross-reacted with full-length,
232 cell-surface expressed BQ.1.1 and XBB.1 S trimers, to levels comparable or greater than those
233 observed for BA.2 S, but not with the E340A S (negative control[48]) escape mutant **(Fig. 3c** and
234 **Extended Data Fig. 5a)**. These data show that sotrovimab IgG binds avidly to all currently
235 dominant Omicron SARS-CoV-2 variants. However, the neutralizing potency of sotrovimab varied
236 widely against these variants, ranging from a 6.5-fold loss against XBB.1 up to a 94-fold loss
237 against BQ.1.1 relative to Wu **(Fig. 3a** and **Extended Data Fig. 6)**, in line with recent
238 reports[1,14,41,46,47].
239 Given the reduced neutralization potency of sotrovimab against these variants despite
240 retaining binding avidity, we evaluated the ability of this therapeutic antibody to activate antibody-
241 dependent cell cytotoxicity (ADCC) using primary natural killer (NK) effector cells and CHO target
242 cells expressing SARS-CoV-2 S of the different Omicron variants at their surface. Sotrovimab
243 efficiently promoted ADCC of cells expressing Wu-D614, BA.2, BQ.1.1 or XBB.1 S in a
244 concentration- and Fc-dependent manner **(Fig. 3d** and **Extended Data Fig. 5b)**. Although we
245 observed a linear relationship between the S309 Fab binding affinity and in vitro neutralization
246 potency, this correlation was not apparent with respect to the magnitude of ADCC, which was
247 equivalent against all variants in spite of up to 100-fold differences in binding affinity **(Fig. 3e)**.
248 To better understand the physiological relevance of these findings, we administered S309
249 to mice which were subsequently challenged with BQ.1.1, the variant associated with the greatest
250 loss of in vitro neutralizing activity (i.e., 94-fold loss relative to Wu-D614 S pseudovirus). S309
251 was given as prophylaxis at 10 or 30 mg/kg doses to K18/hACE2 mice one day prior to challenge
252 with SARS-CoV-2 BQ.1.1. Notably, S309 completely protected K18-hACE2 transgenic mice from
253 weight loss at both doses, whereas animals receiving a control antibody lost greater than 10% of
254 body weight by day 6 **(Fig. 3f)**. Furthermore, S309 administration reduced both viral RNA and
255 infectious virus titers in the lung in a statistically significant manner at both 10 and 30 mg/kg doses
256 relative to control mice **(Fig. 3f)**. These data indicate that, despite its marked reduction of in vitro
257 neutralizing activity, S309 can protect mice from BQ.1.1 challenge (consistent with a recent pre-
258 print on BQ.1.1-challenged hamsters[49]).
259

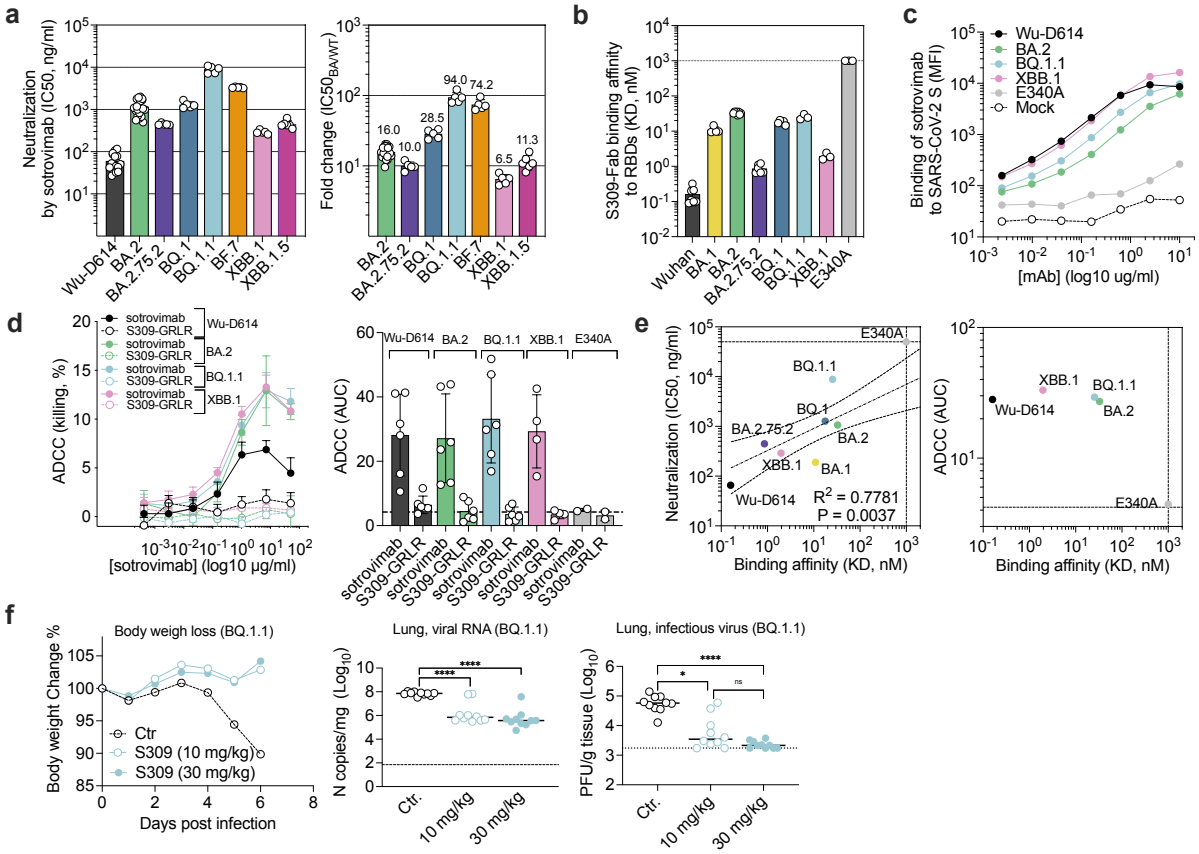

Fig 3. S309 triggers antibody-dependent cell cytotoxicity (ADCC) in vitro and protects mice against BQ.1.1 challenge in vivo. a, Sotrovimab-mediated neutralization of Wu-D614, BA.2, BA.2.75.2, BQ.1, BQ.1.1, BF.7, XBB.1 and XBB.1.5 S VSV pseudoviruses. The sotrovimab neutralizing potency is represented by its IC_{50} (left panel) or fold change relative to neutralization of the Wu-D614 VSV pseudovirus (right panel). Each symbol represents IC_{50} or fold-change values from biological replicates. **b**, Single-cycle kinetics surface plasmon resonance (SPR) analysis of S309 Fab binding to the indicated SARS-CoV-2 RBD variants. Each symbol represents K_D values from independent experiments. **c,** Binding of sotrovimab to SARS-CoV-2 S variants transiently expressed at the surface of Expi-CHO cells as determined by flow-cytometry. Similar levels of variant S expression were confirmed by staining with a monoclonal antibody (S2V29) that retains equal and potent neutralizing activity against Wu-D614, BA.2, BQ.1.1, XBB.1 and E340A (**Extended Data Fig. 5a**). **d**, ExpiCHO-S cells transiently transfected with Wu-D614, BA.2, BQ.1.1 or XBB.1 S were incubated with the indicated concentrations of sotrovimab (derivative of S309) or S309-GRLR mAb and mixed with purified NK cells isolated from healthy donors. Cell lysis was determined by a lactate dehydrogenase release assay. Data are presented as mean values ± standard deviations (SD) from one representative donor (left panel). Area under the curve (AUC) analyses from two, four or six NK donors (right panel). **e**, Correlation of sotrovimab Fab binding affinity with neutralizing activity or ADCC. The neutralization IC_{50} values from (a) or the ADCC AUC values from (d) are plotted on the y-axis and the binding affinity to each RBD variant obtained in (b) is plotted on the x-axis. The neutralization data of S309 against

282 BA.1 were adapted from Cameroni et al. Dotted lines indicate the limit of detection. Best-fit lines
283 were calculated using a simple linear regression. Two-tailed Pearson correlation was used to
284 calculate the R^2 and P values. **f**, Eight-week-old female K18-hACE2 mice received 30 mg/kg of a
285 control isotype-matched monoclonal antibody (anti-West Nile virus hE16), or 10 or 30 mg/kg of
286 S309 (parent of sotrovimab) by intraperitoneal injection one day before intranasal inoculation with
287 10^4 FFU of SARS-CoV-2 BQ.1.1. Body weight loss was monitored daily, and tissues were
288 collected at six days after inoculation. Body weight loss (left panel), lung viral RNA determined by
289 RT-qPCR (middle panel), and infectious lung virus titers was measured by plaque assay (right
290 panel) (lines indicate the median; n = 10 mice per group; Kruskal-Wallis ANOVA with Dunn's post-
291 test between isotype and S309 treatment; ns, not significant; * $P < 0.05$, ****, $P < 0.0001$).
292
293 **Bivalent mRNA vaccines enhance neutralizing antibody responses against emerging**
294 **SARS-CoV-2 variants**
295 To assess the impact of the BQ1.1, XBB.1 and BA.2.75.2 S mutations on vaccine-elicited
296 antibody responses, we quantified plasma neutralizing activity using VSV pseudotyped with Wu-
297 G614, BA.1, BA.5, BF.7, BQ.1.1, XBB.1 or BA.2.75.2 S. We compared plasma from eight cohorts
298 of individuals obtained 15-30 days post vaccination or PCR-confirmed breakthrough (BT) infection
299 corresponding to subjects: (i) mRNA vaccinated four times with the prototype vaccine encoding
300 Wuhan-1 spike and without known infection ("Wu_4 vaccinated"); (ii) mRNA vaccinated four times
301 without known infection, the last dose being the Wu/BA.5 bivalent booster ("Wu/BA.5 bivalent
302 vaccinated"); (iii) previously infected in 2020 (with a WA1/2020–like SARS-CoV-2 strain) and then
303 mRNA vaccinated four to five times, the last dose being Wu/BA.5 mRNA bivalent booster ("pre-
304 Omicron infected-Wu/BA.5 bivalent vaccinated"); (iv) mRNA vaccinated before experiencing an
305 Omicron BA.1, BA.2, BA.2.12.1 or BA.5 BT infection and vaccinated again with the Wu/BA.5
306 mRNA bivalent booster ("Omicron BT-Wu/BA.5 bivalent vaccinated"). As an alternative to the
307 Wu/BA.5 bivalent mRNA booster, Switzerland and a few other countries, offer a Wu/BA.1 bivalent
308 mRNA booster. We therefore analyzed neutralization in additional cohorts: (v) mRNA vaccinated
309 three times with the Wu monovalent vaccine without known infection ("Wu_3 vaccinated"); (vi)
310 mRNA vaccinated three times with the Wu monovalent vaccine after pre-Omicron BT infection
311 ("pre-Omicron infected-Wu vaccinated"); (vii) mRNA vaccinated four times without known
312 infection, the last dose being the Wu/BA.1 bivalent booster ("Wu/BA.1 bivalent vaccinated"); (viii)
313 mRNA vaccinated four times with a BA.1 or a BA.2 BT infection, the last dose being the Wu/BA.1
314 bivalent booster ("Omicron BT-Wu/BA.1 bivalent vaccinated"). In addition, we analyzed plasma
315 samples obtained from kidney transplant recipients (KTR) vaccinated with four Wu monovalent
316 doses with or without pre-Omicron infection.
317 Wu/BA.5 or Wu/BA.1 bivalent mRNA vaccination elicited comparable neutralizing
318 antibody titers against Wu-G614 S VSV with that observed in matched Wu vaccinated cohorts
319 but higher neutralization of BA.1 S and BA.5 S VSV pseudoviruses **(Fig. 4 a, b)**. Cohorts that
320 received the Wu/BA.5 or the Wu/BA.1 bivalent mRNA vaccines had detectable neutralizing
321 activity against the vaccine-mismatched XBB.1, BA.2.75.2 and BQ.1.1 S VSV pseudoviruses,
322 irrespective of prior infection status, whereas little to no neutralization of these variants was
323 detected for the Wu-only vaccinated subjects **(Fig. 4 a, b).** We did not detect plasma neutralizing
324 activity against circulating Omicron variants in subjects that were vaccinated four times with the
325 Wu monovalent booster but were immunosuppressed following kidney transplantation,

326 underscoring the difficulties associated with protecting these at-risk populations (**Extended Data**
327 **Fig. 7**). Overall, these data suggest that bivalent (Wu/BA.1 or Wu/BA.5) mRNA vaccination elicits
328 more potent and broader antibody responses against vaccine-matched and mismatched Omicron
329 variants than Wu mRNA vaccination in healthy subjects.
330
331 **Plasma antibodies maintain binding and Fc-mediated effector function against emerging**
332 **Omicron variants**
333 Next, we investigated binding and Fc-mediated effector function of plasma antibodies from
334 cohorts v to viii. The progressive reduction of neutralizing antibody titers against currently
335 dominant Omicron variants overtime was not paralleled by a similar decrease in IgG binding titers
336 to matched RBDs (**Fig. 4c**), as binding titers remained comparable across all Omicron variants.
337 This finding is consistent with data on pre-Omicron variants[50] and with the notion that SARS-CoV-
338 2 is evolving primarily to escape from neutralizing antibodies that exert the greatest selective
339 pressure.
340 Fc-mediated effector function of plasma antibodies was evaluated by measuring activation
341 of the FcγRIIIa (V158 allele) as a surrogate of ADCC using Jurkat reporter cells and Wu-G614,
342 BA.5, BQ.1.1 and XBB.1 SARS-CoV-2 S-expressing ExpiCHO as target cells (**Fig. 4d** and
343 **Extended Data Fig. 8**). Each cohort exhibited high individual variability in the ability of plasma to
344 trigger activation of FcγRIIIa, with some donors lacking measurable activity despite the presence
345 of high titers of RBD-binding antibodies (**Fig. 4c**). Samples that scored positive for FcγRIIIa
346 triggering against Wu retained activity against BA.5, BQ.1.1 and XBB.1 S variants. These results
347 suggest that antibodies capable of triggering Fc effector functions vary widely amongst
348 individuals, but, when present, these antibodies are broadly reactive against Omicron variants.
349
350
351

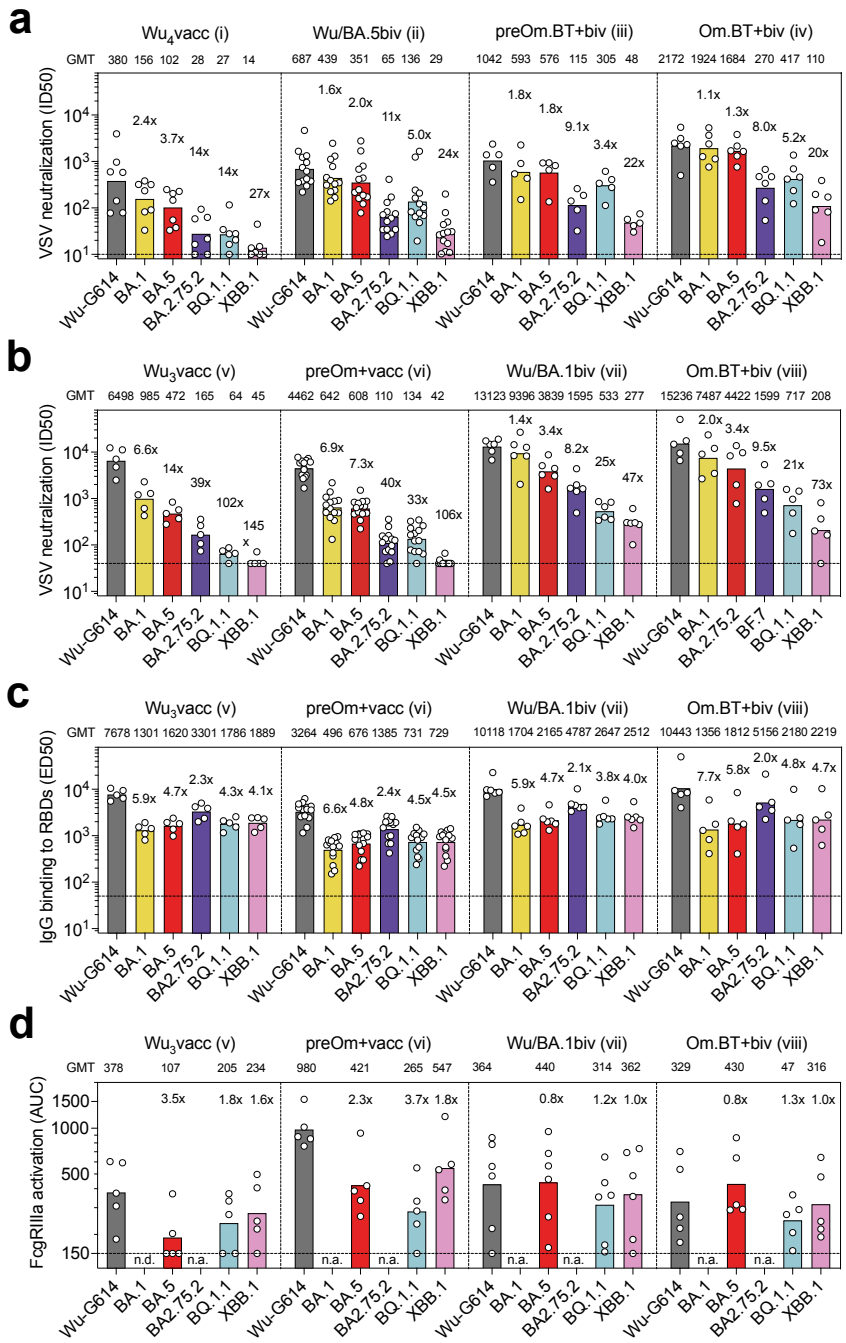

Fig. 4. Neutralization, binding and Fc-dependent effector functions of vaccine-elicited plasma antibodies against the BA.2.75.2, BQ.1.1 and XBB.1 variants. a, b, Neutralization of SARS-CoV-2 pseudotyped VSV carrying Wu-G614, Omicron BA.1, BA.5, BA.2.75.2, BQ.1.1 and XBB.1 S by plasma samples of cohorts i-iv (a) and v-viii (b). Plasma neutralizing titers expressed as ID_{50}s from n = 2 biological (a) and technical (b) replicates are shown. Bars and values on top represent geometric mean ID_{50} titers (GMT). Fold-loss of neutralization against Omicron variants as compared to Wu-G614 is shown above each corresponding bar. Horizontal dashed lines indicate the limit of detection in these assays (ID_{50} = 10 in panel a and 40 in panel b). **c,** Binding of plasma IgG antibodies to SARS-CoV-2 RBDs from Wu, Omicron BA.1, BA.5, BA.2.75.2, BQ.1.1

362 and XBB.1 variants as measured by ELISA. Shown are ED_{50} values from n = 2 technical replicates
363 of samples from cohorts v-viii. Bars represent geometric mean ED_{50} binding titers (GMT). Fold-
364 loss of binding titers to Omicron variants as compared to Wu is shown above each corresponding
365 bar. Horizontal dashed line indicates the limit of detection (ED_{50} = 50). **d,** Activation of FcγRIIIa
366 (V158 allele) measured using Jurkat reporter cells and Wu-G614, BA.5, BQ.1.1 and XBB.1 SARS-
367 CoV-2 S glycoprotein-expressing ExpiCHO as target cells. Shown are AUC values from one
368 experiment with plasma samples from cohorts v-viii (n=5 donors for cohort v, n=5 for cohort vi,
369 n=6 for cohort vii and n=5 for cohort viii). Bars and values on top represent geometric mean AUC
370 titers (GMT). Fold-change of activation with Omicron variants as compared to Wu-G614 is shown
371 above each corresponding bar. The horizontal dashed line indicates the limit of detection (AUC =
372 150). n.a., not assayed. Demographics of cohorts are summarized in **Supplementary Table 5**.
373
374 **Cross-reactive RBD-specific memory B cells dominate bivalent vaccine-elicited responses**
375 We next compared memory B cell (MBC) populations in the Wu_4 vaccinated, Wu/BA.5
376 bivalent vaccinated (including one individual [31H] who received the Janssen COVID-19 vaccine
377 as their first vaccine series), pre-Omicron infected-Wu/BA.5 bivalent vaccinated, and Omicron
378 BT-Wu/BA.5 bivalent vaccinated subjects (cohorts i-iv) by enumerating the frequency of Wu RBD-
379 specific, Omicron RBD-specific (pool of BA.1/BA.2/BA.5), and cross-reactive MBCs by flow
380 cytometry. Individuals who were exposed only to Wu S through vaccination (Wu_4 vaccinated) had
381 the highest frequency of Wu RBD-specific MBCs (mean frequency: 25.8%) and the lowest
382 frequency of cross-reactive MBCs (mean frequency: 71.1%) of the four cohorts examined **(Fig.**
383 **5a, b** and **Extended Data Fig. 9)**. Individuals who were exposed only once to Omicron S through
384 vaccination had few Omicron RBD-specific MBCs (mean frequency: 5.1%), regardless of whether
385 they had experienced a pre-Omicron SARS-CoV-2 infection (Wu/BA.5 bivalent and pre-Omicron
386 bivalent). Most RBD-specific MBCs in these cohorts cross-reacted with the Wu RBD and the
387 Omicron RBD pool (BA.1/BA.2/BA.5), with uninfected individuals having similar frequencies of
388 cross-reactive MBCs (mean: 77.4%) when compared to individuals who had experienced a pre-
389 Omicron infection (mean frequency: 77.1%) **(Fig. 5a, b** and **Extended Data Fig. 9)**. These data
390 are consistent with previous analyses of MBC populations in Wu vaccinated individuals who had
391 experienced an Omicron BT infection and suggest that immunological imprinting limits the
392 development of new Omicron-specific MBCs, although there is efficient recall of cross-reactive
393 MBCs after a single exposure to Omicron S[1,43,51]. Although Omicron BT-Wu/BA.5 bivalent
394 vaccinated subjects had two exposures to an Omicron S (one through infection and one through
395 vaccination), they still had relatively few Omicron-specific MBCs (mean: 5.3%) similar to those
396 individuals who received only the bivalent booster. The Wu/Omicron (BA.1/BA.2/BA.5) RBD pool
397 cross-reactive MBCs were further enriched (mean frequency: 81.5%) for this cohort compared to
398 the Wu/BA.5 bivalent vaccinated cohort **(Fig. 5a, b** and **Extended Data Fig. 9)**.
399 To assess the ability of MBCs to recognize the currently circulating Omicron variants, we
400 examined whether MBCs recognizing the Omicron RBD pool (including those that are cross-
401 reactive with the Wu RBD and those that are not) could bind the BQ.1.1 RBD (**Fig. 5c** and
402 **Extended Data Fig. 10a, b**). Most Wu/Omicron RBD pool cross-reactive memory B cells
403 recognized the BQ.1.1 RBD (mean frequency: 66.3%), whereas only a small fraction of MBCs
404 binding to the Omicron RBD pool and not the Wu RBD also recognized the BQ.1.1 RBD (mean
405 frequency: 16.9%), regardless of infection and vaccination status. These Omicron-specific MBCs

were likely elicited de novo upon Omicron S exposure (through infection and/or vaccination) and their breadth towards currently dominant Omicron variants may improve over time through affinity maturation, similar to the maturation of the antibody response observed after infection with the SARS-CoV-2 Wu or Washington-1 strain or vaccination[30,52–59].

We next determined if the BA.5 versus BA.1 formulations of bivalent boosters differentially affected the composition of the RBD-specific MBC population (**Fig. 5d-f** and **Extended Data Fig. 10 c,d**). The cross-reactivity of IgGs secreted by in vitro stimulated memory B cells to the Wu, BA.1, BQ.1.1 and XBB.1 RBDs was assessed following Wu/BA.1 bivalent vaccination for uninfected individuals and individuals who had experienced an Omicron BT infection (cohorts vii and viii). Vaccination with the Wu/BA.1 bivalent booster did not elicit Omicron RBD-specific MBCs in either the uninfected or Omicron-BT cohorts. Most RBD-specific antibodies were found to be cross-reactive with BA.1 regardless of infection status (mean frequencies: 76.3% in uninfected and 73.6% in Omicron BT infected subjects), whereas a lower fraction cross-reacted with BQ.1.1 (59.9% and 57.4%) and XBB.1 RBDs (55.9% and 57.4%).

Collectively, these data suggest that two Omicron S exposures are not sufficient to overcome the immunological imprinting induced by repeated Wu S exposures but does continue to enrich for MBCs cross-reacting with multiple RBD variants.

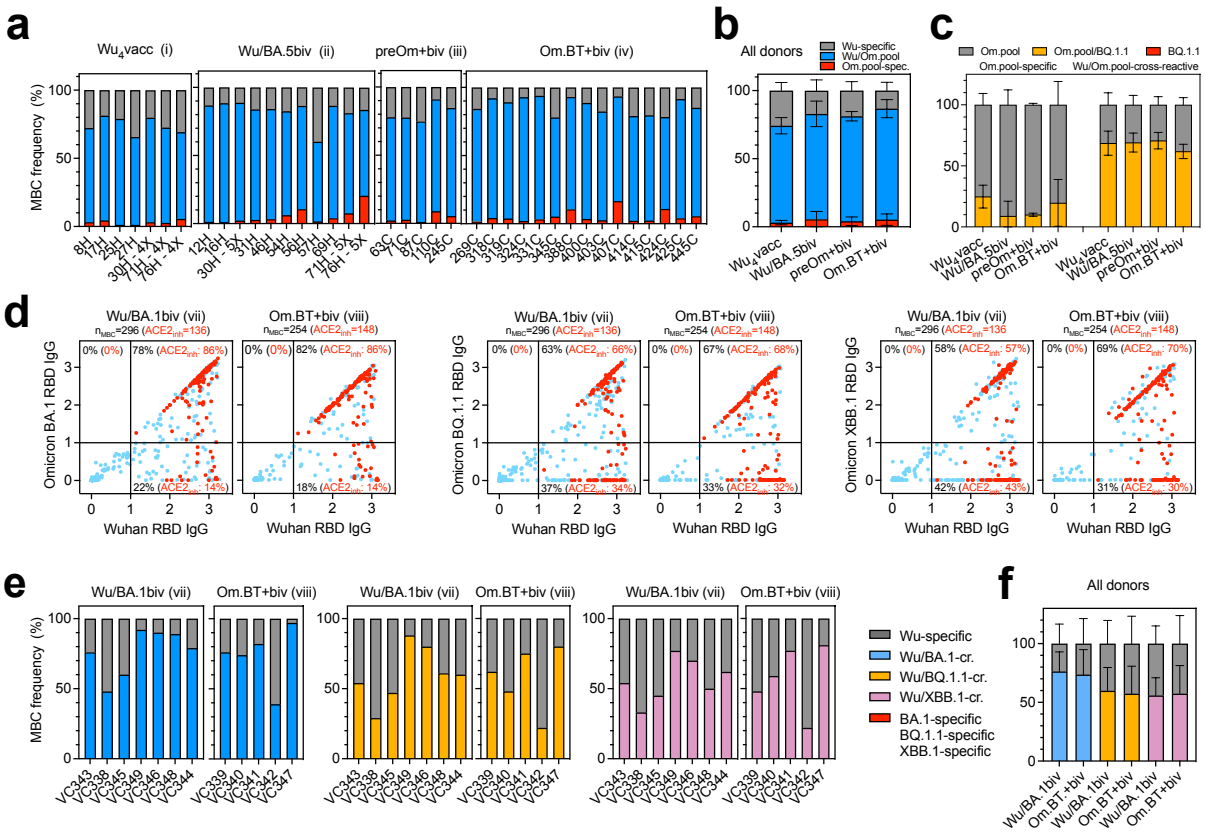

Figure 5. Cross-reactivity of vaccine-elicited SARS-CoV-2 RBD-specific MBCs. a, b, Frequency of Wu RBD-specific (grey), Omicron (BA.1/BA.2/BA.5) RBD pool-specific (red) and Wu/Omicron RBD pool-cross-reactive (blue) MBCs from donors of cohorts i-iv, as measured by flow cytometry. Individual frequencies and mean ± SD are shown in panels a and b, respectively.

429 **c**, Analysis of cross-reactivity with the BQ.1.1 RBD of Omicron RBD pool-specific (red bars of
430 panel b) and Wu/Omicron RBD-cross-reactive (blue bars of panel b) MBCs. Om.pool, MBCs
431 recognizing the Omicron (BA.1/BA.2/BA.5) RBD pool. **d**, Cumulative cross-reactivity of IgGs
432 secreted from in vitro stimulated MBCs between the Wu RBD and the Omicron BA.1, BQ.1.1 or
433 XBB.1 RBDs as measured by ELISA. Data represent average OD values with blank subtracted
434 from n = 2 replicates of MBC cultures analyzed from donors of cohorts vii and viii. RBD-specific
435 IgGs showing inhibition of binding to ACE2 are depicted in red. Number of total and ACE2-
436 inhibiting ($ACE2_{inh}$) RBD-directed IgG positive cultures are indicated on top of each graph.
437 Percentages of Wu-specific, Omicron-specific and Wu/Omicron-cross-reactive IgG positive
438 cultures are indicated within each quadrant. **e, f**, Individual frequencies and mean frequencies ±
439 SD of Wu RBD-specific (grey), Omicron-specific (red) and Wu/Omicron RBD cross-reactive (blue
440 for BA.1, yellow for BQ.1.1 and purple for XBB.1) IgG positive cultures from donors of cohorts vii
441 and viii are shown in panels **e** and **f**, respectively.
442
443 **Discussion**
444 SARS-CoV-2 evolution is driven by viral immune escape and transmissibility[60,61]. The
445 Omicron BA.1, BA.2 and BA.5 lineages, which led to successive waves of infection over the past
446 year, were characterized by immune evasion from Wu S-elicited neutralizing antibodies, higher
447 ACE2-binding affinity, impaired S-mediated fusogenicity and a change in entry pathway due to
448 reduced TMPRSS2-dependence[3–15,39]. Here, we report that the recently emerged SARS-CoV-2
449 Omicron variants have an unprecedented level of immune evasion with reduction of neutralizing
450 antibody titers reaching up to 100-fold for XBB.1. Whereas BQ.1.1 and BA.2.75.2 retained the
451 high ACE2 binding affinity, similar to earlier Omicron variants, XBB.1 has a lower affinity,
452 comparable to that of the Wu RBD. Although XBB.1 is the most immune evasive of these three
453 Omicron variants, its reduced affinity for ACE2 relative to other co-circulating strains may have
454 hindered its spread. The enhanced ACE2 binding affinity of the newly emerging XBB.1.5, which
455 harbors the S486P RBD mutation (relative to BA.2), may explain the current spread of this rapidly
456 rising variant[47]. We also demonstrate that BQ.1.1 and XBB.1 S display an increased resistance
457 to protease inhibitors blocking membrane or endosomal viral entry relative to other Omicron
458 lineages, suggesting peculiar alterations in the viral entry process of these variants. Collectively,
459 these findings illustrate the complex interplay of immune evasion, fusogenicity and ACE2 affinity
460 in driving SARS-CoV-2 evolution.
461 There is growing evidence that multiple mechanisms can contribute to protection from
462 infection and severe disease, including humoral and cellular responses[26,62–65]. In particular,
463 antibody-dependent cell cytotoxicity (ADCC) and antibody-dependent opsonophagocytosis are
464 Fc-mediated effector functions that can promote virus clearance and enhance adaptive immune
465 responses in vivo, independently of direct viral neutralization. In this context, it is intriguing that
466 both neutralizing and binding antibody titers were reported as correlates of protection in a phase
467 3 study[66]. We recently showed that sotrovimab (S309) retained in vitro effector functions against
468 BA.2 and conferred Fc-dependent protection in the lungs of mice infected with BA.2[67]. This
469 preclinical finding is supported by the accumulation of real-world evidence suggesting that
470 adverse clinical outcomes, such as hospitalization and mortality, remained consistently low during
471 the BA.2 wave in patients treated with sotrovimab[68–72]. Here, we show that sotrovimab retained in
472 vitro effector functions against all Omicron variants at levels comparable to those observed with

Wu. Importantly, despite 94-fold reduced in vitro neutralizing activity, prophylactic administration of S309 (sotrovimab parent) protected mice against BQ.1.1 challenge, suggesting that Fc-dependent effector functions can compensate for substantial losses of neutralizing activity. Our observation that vaccine-elicited polyclonal plasma antibodies cross-react and trigger FcγRIIIa signaling, as a surrogate of ADCC, upon recognition of the BQ.1.1 and XBB.1 S glycoproteins, concur with observations made with prior Omicron variants[73–75] and further hint at a protective role for broadly reactive antibodies with effector functions. Our findings are consistent with a model in which the erosion of neutralizing antibody titers due to viral immune evasion is associated with increased frequency of breakthrough infections, while the persistence of functional cross-reactive antibodies contributes to protection against severe COVID-19[76].

Immune imprinting, also termed original antigenic sin, was first described in 1960 based on the observation that influenza virus infection with a strain distinct from prior exposures preferentially boosted antibody responses against epitopes shared with the original strain instead of inducing responses against the new strain[77]. Analysis of the specificity of antibodies secreted by plasmablasts obtained approximately 1-2 weeks following infection with the antigenically-shifted 2009 H1N1 swine origin pandemic influenza virus revealed a recall of pre-existing, cross-reactive memory B cells[78,79]. Conversely, antibodies secreted by plasma cells and memory B cells[80] obtained from the same individuals after seasonal influenza vaccination, corresponding to a second antigenic exposure, were subtype-specific (i.e., targeting non-conserved epitopes). We and others previously showed that Omicron breakthrough infections of Wu-vaccinated subjects primarily recall cross-reactive memory B cells specific for epitopes shared by multiple SARS-CoV-2 variants rather than priming naïve B cells recognizing Omicron RBD-specific epitopes[1,43,51]. Unexpectedly, we observed a low to undetectable number of MBCs specific for Omicron RBDs, and not cross-reacting with the Wu RBD, even after two exposures to Omicron S antigens, including with Wu/BA.5 or Wu/BA.1 bivalent mRNA vaccination. This observation may be explained by a combination of strong immune imprinting and by the antigenic dominance of Wu antigens in bivalent vaccines. This mechanism is reminiscent of current efforts to develop universal influenza vaccines to elicit cross-reactive antibodies by serial stimulation with heterologous chimeric hemagglutinins[81]. As expected, however, we found that bivalent Wu/BA.5 mRNA vaccination enriches for MBCs that are cross-reactive with the vaccine-matched and mismatched RBD variants, relative to monovalent Wu mRNA vaccination. The identification of suitable strategies to design broadly protective vaccines against sarbecoviruses[21,22,82–88] and the development of mucosal vaccines[89–91] may result in the development of variant-proof SARS-CoV-2 vaccines through the elicitation of functional cross-reactive antibodies.

515 # Methods

516 ## Cells and Viruses

517 Cell lines used in this study were obtained from ATCC (HEK293T and VeroE6), Thermo Fisher
518 Scientific (Expi-CHO-S cells, FreeStyle 293-F cells and Expi293F cells), Takara (Lenti-X 293T
519 cells), kindly gifted from Jesse Bloom (HEK293T-ACE2), or generated in lab (BHK-21-GFP_{1-10} or
520 VeroE6-TMPRSS2-GFP_{11}). None of the cell lines used were authenticated nor tested for
521 mycoplasma contamination.

522

523 ## Sample donors

524 Samples were obtained from SARS-CoV-2 convalescent and vaccinated individuals under study
525 protocols approved by the local institutional review boards (Canton Ticino and Canton Aargau
526 Ethics Committees, Switzerland). All donors provided written informed consent for the use of
527 blood and blood derivatives (such as peripheral blood mononuclear cells, sera or plasma) for
528 research. Sera and peripheral blood mononuclear cells (PBMCs) from individuals who received
529 the Wuhan-Hu-1/BA.5 bivalent mRNA vaccines were obtained from the HAARVI study approved
530 by the University of Washington Human Subjects Division Institutional Review Board
531 (STUDY00000959). Demographic data for these individuals is presented in **Supplementary**
532 **Tables 5 and 6.**

533

534 ## Constructs

535 The full-length Wuhan-Hu-1/G614, Delta, BA.1, BA.2, and BA.4/5 S constructs with a 21 amino
536 acid C-terminal deletion used for pseudovirus were previously described elsewhere (). The full-
537 length BA.2.75.2 and XBB.1 S constructs containing a 21 amino acid C-terminal deletion were
538 codon-optimized, synthesized, and inserted the HDM vector by Genscript. The full-length BQ.1.1
539 S construct containing a 21 amino acid C-terminal deletion was generated by mutagenesis of the
540 BA.4/5 S construct by Genscript.

541 The SARS-CoV-2 Wuhan-Hu-1 RBD construct containing an N-terminal mu-phosphatase
542 secretion signal and a C-terminal octa-histidine tag followed by flexible linker and Avi tag was
543 previously described elsewhere. The BA.4/5 RBD construct containing an N-terminal BM40
544 secretion tag and a C-terminal octa-histidine tag followed by flexible linker and Avi tag was
545 previously described elsewhere. The BA.2.75.2, BQ.1.1, and BA.4/5 RBD constructs containing
546 an N-terminal BM40 secretion tag and a C-terminal octa-histidine tag followed by flexible linker
547 and Avi tag were codon optimized, synthesized, and inserted into the pcDNA3.1(+) vector by
548 Genscript. The boundaries of the construct are N-328RFPN331 and 528KKST531-C.

549

550 ## Generation of VSV pseudovirus

551 Replication defective VSV pseudovirus expressing SARS-CoV-2 spike proteins corresponding to
552 the ancestral Wuhan-Hu-1 virus and the VOCs were generated as previously described (*3*), with
553 some modifications. Lenti-X 293T cells (Takara) were seeded in 15-cm^2 dishes at a density of
554 10×10^6 cells per dish and the following day were transfected with 25 µg of spike expression
555 plasmid with TransIT-Lenti (Mirus, 6600) according to the manufacturer's instructions. One day
556 after transfection, cells were infected with VSV-luc (VSV-G) with a multiplicity of infection (MOI)

557 of 3 for 1 h, rinsed three times with PBS containing Ca2+ and Mg2+, then incubated for an
558 additional 24 h in complete medium at 37 °C. The cell supernatant was clarified by centrifugation,
559 aliquoted, and frozen at −80 °C. Spike expression plasmids used for the generation of VSV
560 pseudoviruses carry the following mutations: BA.1: A67V, Δ69-70, T95I, G142D, Δ143-145,
561 Δ211, L212I, ins214EPE, G339D, S371L, S373P, S375F, K417N, N440K, G446S, S477N,
562 T478K, E484A, Q493R, G496S, Q498R, N501Y, Y505H, T547K, D614G, H655Y, N679K, P681H,
563 N764K, D796Y, N856K, Q954H, N969K, L981F; BA.2: T19I, L24-, P25-, P26-, A27S, G142D,
564 V213G, G339D, S371L, S373P, S375F, D405N, R408S, K417N, N440K, S477N, T478K, E484A,
565 Q493R, Q498R, N501Y, Y505H, D614G, H655Y, N679K, P681H, N764K, D796Y, N856K,
566 Q954H, N969K; K417N, N440K, G446S, N460K, S477N, T478K, E484A, Q498R, N501Y, Y505H,
567 D614G, H655Y, N679K, P681H, N764K, D796Y, Q954H, N969K; BA.2.75.2: T19I, L24-, P25-,
568 P26-, A27S, G142D, K147E, W152R, F157L, I210V, V213G, G257S, G339H, R346T, S371F,
569 S373P, S375F, T376A, D405N, R408S, K417N, N440K, G446S, N460K, S477N, T478K, E484A,
570 F486S, Q498R, N501Y, Y505H, D614G, H655Y, N679K, P681H, N764K, D796Y, Q954H, N969K,
571 D1199N; BQ.1: T19I, L24-, P25-, P26-, A27S, Δ69-70, G142D, V213G, G339D, S371F, S373P,
572 S375F, T376A, D405N, R408S, K417N, N440K, K444T, L452R, N460K, S477N, T478K, E484A,
573 F486V, Q498R, N501Y, Y505H, D614G, H655Y, N679K, P681H, N764K, D796Y, Q954H, N969K;
574 BQ.1.1: T19I, L24-, P25-, P26-, A27S, Δ69-70, G142D, V213G, G339D, R436T, S371F, S373P,
575 S375F, T376A, D405N, R408S, K417N, N440K, K444T, L452R, N460K, S477N, T478K, E484A,
576 F486V, Q498R, N501Y, Y505H, D614G, H655Y, N679K, P681H, N764K, D796Y, Q954H, N969K;
577 BF.7: T19I, L24-, P25-, P26-, A27S, Δ69-70, G142D, V213G, G339D, R436T, S371F, S373P,
578 S375F, T376A, D405N, R408S, K417N, N440K, L452R, S477N, T478K, E484A, F486V, Q498R,
579 N501Y, Y505H, D614G, H655Y, N679K, P681H, N764K, D796Y, Q954H, N969K; XBB.1: T19I,
580 L24-, P25-, P26-, A27S, V83A, G142D, Y144-, H146Q, Q183E, V213E, G252V, G339H, R346T,
581 L368I, S371F, S373P, S375F, T376A, D405N, R408S, K417N, N440K, V445P, G446S, N460K,
582 S477N, T478K, E484A, F486S, F490S, Q498R, N501Y, Y505H, D614G, H655Y, N679K, P681H,
583 N764K, D796Y, Q954H, N969K; XBB.1.5: T19I, L24-, P25-, P26-, A27S, V83A, G142D, Y144-,
584 H146Q, Q183E, V213E, G252V, G339H, R346T, L368I, S371F, S373P, S375F, T376A, D405N,
585 R408S, K417N, N440K, V445P, G446S, N460K, S477N, T478K, E484A, F486P, F490S, Q498R,
586 N501Y, Y505H, D614G, H655Y, N679K, P681H, N764K, D796Y, Q954H, N969K

587 Pseudotyped VSV was produced as previously described. Briefly, HEK293T were split into poly-
588 D-lysine coated 15 cm plates and grown overnight until they reached approximately 70-80%
589 confluency. The cells were washed 3 times with Opti-MEM (Gibco) and transfected with either the
590 Wuhan-Hu-1(D614), Wu-G614, Delta, BA.1, BA.2, BA.4/5, BA.2.75.2, BQ.1.1, or XBB.1 S
591 constructs using Lipofectamine 2000 (Life Technologies). After 4-6 hours, the media was
592 supplemented with an equal volume of DMEM supplemented with 20% FBS and 2% PS. The
593 cells were incubated for 20-24 hours, washed 3 times with DMEM, and infected with VSVΔG-luc.
594 Two hours after VSVΔG-luc infection, the cells were then washed an additional five times with
595 DMEM. The cells were grown in DMEM (for virus stocks used in sotrovimab neutralization assays)
596 or in DMEM supplemented with anti-VSV-G antibody (I1-mouse hybridoma supernatant diluted
597 1:25, from CRL-2700, ATCC) for 18-24 hours, after which the supernatant was harvested and
598 clarified by low-speed centrifugation at 2,500 g for 10 min. The supernatant was then filtered (0.45
599 µm) and some virus stocks were concentrated 10 times using a 30 kDa centrifugal concentrator
600 (Amicon Ultra). The pseudotyped viruses were then aliquoted and frozen at -80°C.

601

602 **VSV pseudovirus neutralization**

603 Vero E6 cells were grown in DMEM supplemented with 10% FBS and seeded into white-walled
604 96 well plates (PerkinElmer, 6005688) at a density of 20,000 cells per well. The next day,
605 monoclonal antibodies were serially diluted in pre-warmed complete medium, mixed with
606 pseudoviruses and incubated for 1 h at 37 °C in round bottom polypropylene plates. Medium from
607 cells was aspirated and 50 µl of virus–monoclonal antibody complexes were added to cells, which
608 were then incubated for 1 h at 37 °C. An additional 100 µl of pre-warmed complete medium was
609 then added on top of complexes and cells were incubated for an additional 16–24 h. Conditions
610 were tested in duplicate or triplicate wells on each plate and 6-8 wells per plate contained
611 untreated infected cells (defining the 0% of neutralization, 'MAX RLU' value) and uninfected cells
612 (defining the 100% of neutralization, 'MIN RLU' value). Virus–monoclonal antibody-containing
613 medium was then aspirated from cells and 50 or 100 µl of a 1:2 dilution of SteadyLite Plus
614 (PerkinElmer) or BioGlo (Promega) in PBS with Ca^{2+} and Mg^{2+} was added to cells. Plates were
615 incubated for 15 min at room temperature and then analyzed on the Synergy-H1 (Biotek). The
616 average relative light units (RLUs) of untreated infected wells (MAX RLUave) were subtracted by
617 the average of MIN RLU (MIN RLUave) and used to normalize percentage of neutralization of
618 individual RLU values of experimental data according to the following formula: (1 − (RLUx –
619 MIN RLUave)/ (MAX RLUave – MIN RLUave)) × 100. Data were analyzed with Prism (v.9.1.0).
620 IC_{50} values were calculated from the interpolated value from the log(inhibitor) versus response,
621 using variable slope (four parameters) nonlinear regression with an upper constraint of <100.
622 Each neutralization experiment was conducted on at least two independent experiments – that is,
623 biological replicates – in which each biological replicate contains a technical duplicate or triplicate.

624 VeroE6-TMPRSS2 were split into white-walled, clear bottom 96 well plates (Corning) and grown
625 overnight until they reached approximately 70% confluency. Sera (or plasma) were diluted in
626 DMEM starting at a 1:33 or 1:66 dilution and serially diluted in DMEM at a 1:3 dilution thereafter.
627 Pseudotyped VSV was diluted at a 1:25 to 1:100 ratio in DMEM and an equal volume was added
628 to the diluted sera. The virus-sera mixture was incubated for 30 minutes at room temperature and
629 added to the VeroE6-TMPRSS2 cells. After two hours, an equal volume of DMEM supplemented
630 with 20% FBS and 2% PS was added to the cells. After 20-24 hours, ONE-Glo EX (Promega)
631 was added to each well and the cells were incubated for 5 minutes at 37ºC. Luminescence values
632 were measured using a BioTek plate reader. Luminescence readings from the neutralization
633 assays were normalized and analyzed using GraphPad Prism 9. The relative light unit (RLU)
634 values recorded from uninfected cells were used to define 100% neutralization and RLU values
635 recorded from cells infected with pseudovirus without sera or antibodies were used to define 0%
636 neutralization. ID50 were determined from the normalized data points using a [inhibitor] vs.
637 normalized response – variable slope model using at least two technical repeats to generate the
638 curve fits. At least two biological replicates with two distinct batches of pseudovirus were
639 conducted for each sample.

640

641 **Pseudotyped VSV entry assays with protease inhibitors**

642 VeroE6-TMPRSS2 or HEK293T-ACE2 were split into white-walled, clear bottom 96 well plates
643 (Corning) at a density of 18,000 or 36,000 cells, respectively, and grown overnight. The following

644 day, the growth media was removed and, for assays conducted with VeroE6-TMPRSS2, the cells
645 washed once with DMEM. The cells were incubated for 2 hours with DMEM containing 50 μM of
646 Camostat (Sigma), Nafamostat (Sigma), E-64d (Sigma), or 0.5% DMSO. All three protease
647 inhibitors were dissolved in DMSO to a concentration of 10 mM and diluted in DMEM. The
648 protease inhibitors were removed and pseudovirus diluted 1:50 or 1:200 in DMEM was added to
649 the cells. After two hours, an equal volume of DMEM supplemented with 20% FBS and 2% PS
650 was added to the cells. After 20-24 hours, ONE-Glo EX (Promega) was added to each well and
651 the cells were incubated for 5 minutes at 37ºC. Luminescence values were measured using a
652 BioTek plate reader. Luminescence readings from the neutralization assays were normalized and
653 analyzed using GraphPad Prism 9. The RLU values recorded from uninfected cells were used to
654 define 0% infectivity and RLU values recorded from cells incubated with 0.5% DMSO only and
655 infected with pseudovirus were used to define 100% infectivity. Twelve technical replicates were
656 performed for each inhibitor and pseudovirus and at least two biological replicates with two distinct
657 batches of pseudovirus were conducted.
658

659 **Recombinant protein production for BLI, FACS, and cryoEM**

660 SARS-CoV-2 RBD proteins were produced and purified from Expi293F cells as previously
661 described. In brief, cells were grown to a density of 3 x 10^6 cells/mL and transfected using the
662 ExpiFectamine 293 Transfection Kit (ThermoFisher Scientific). Three to 5 days post-transfection,
663 proteins were purified from clarified supernatants using HisTrap HP affinity columns (Cytiva) and
664 washed with ten column volumes of 20 mM imidazole, 25 mM sodium phosphate pH 8.0, and 300
665 mM NaCl before elution on a gradient to 500 mM imidazole, 25 mM sodium phosphate pH 8.0,
666 and 300 mM NaCl. Proteins were buffer exchanged into 20 mM sodium phosphate pH 8 and 100
667 mM NaCl and concentrated using centrifugal filters (Amicon Ultra) before being flash frozen. For
668 cryo-EM, recombinant ACE2 (residues 19-615 from Uniprot Q9BYF1 with a C-terminal thrombin
669 cleavage site-TwinStrep-10xHis-GGG-tag, and N-terminal signal peptide) was expressed in
670 ExpiCHO-S cells at 37°C and 8% CO_2 with kifunensine added to 10 μM. Cell culture supernatant
671 was collected eight days post transfection, supplemented with buffer to a final concentration of 80
672 mM Tris-HCl pH 8.0, 100 mM NaCl, and then incubated with BioLock (IBA GmbH) solution. ACE2
673 was purified using a 5 mL StrepTrap HP column (Cytiva) followed by isolation of the monomeric
674 ACE2 by size exclusion chromatography using a Superdex 200 Increase 10/300 GL column
675 (Cytiva) pre-equilibrated in PBS. Recombinant S309 Fab used for cryo-EM was expressed in
676 HEK293 suspension cells, purified using CaptureSelect IgG-CH1 resin and buffer exchanged into
677 PBS (ATUM Bio).
678

679 **Biolayer interferometry**

680 Biotinylated Wu, BA.4/5, BA.2.75.2, BQ.1.1, and XBB.1 RBDs were diluted to a concentration of
681 5 ng/μL in 10X kinetics buffer and loaded onto pre-hydrated streptavidin biosensors to a 1 nm
682 total shift. The loaded tips were dipped into a 1:3 dilution series of monomeric human ACE2
683 starting at 900 nM or 300 nM for 300 seconds followed by dissociation in 10X kinetics buffer for
684 300 seconds. All steps of the affinity measurements using biolayer interferometry were carried
685 out at 30ºC with a shaking speed of 1,000 rpm.
686

687 **Surface plasmon resonance to measure binding of RBDs with ACE2**
688 Measurements were performed using a Biacore T200 instrument. Experiments were performed
689 at 25°C, with the samples held at 15°C in the instrument prior to injection. A CM5 chip with
690 covalently immobilized anti-Avi polyclonal antibody (GenScript, Cat #: A00674-40) was used for
691 surface capture of His-Avi tag containing RBDs. Running buffer was 1x HBS-EP+ pH 7.4 (10 mM
692 HEPES, 150 mM NaCl, 3 mM EDTA and 0.05% v/v Surfactant P20) (Cytiva, Cat #: BR100669).
693 Experiments were performed with a 4-point dilution series of monomeric S309 Fab or monomeric
694 Strep-tagged ACE2 starting at 300nM. The dilution factors are 3-fold (300, 100, 33.3, 11,1nM),
695 3.25-fold (300, 92.3, 28.4, 8.7nM) or 4-fold (300, 75, 18.8, 4.7nM). Experiments were run as
696 single-cycle kinetics, n=2-14 for each RBD ligand. Data were double reference-subtracted and fit
697 to a binding model using Biacore Evaluation software. The 1:1 binding model was used to
698 determine the kinetic parameters. Kinetic values out of the instrument's limit were omitted. K_D
699 values are reported as the average of all replicates with the corresponding standard deviation
700 (**Supplementary Table 2**).
701
702 **In vivo studies**
703 Animal studies were carried out in accordance with the recommendations in the Guide for the
704 Care and Use of Laboratory Animals of the National Institutes of Health. The protocols were
705 approved by the Institutional Animal Care and Use Committee at the Washington University
706 School of Medicine (assurance number A3381–01). Virus inoculations were performed under
707 anesthesia that was induced and maintained with ketamine hydrochloride and xylazine, and all
708 efforts were made to minimize animal suffering. Heterozygous K18-hACE2 C57BL/6 J mice
709 (strain: 2B6.Cg-Tg(K18-ACE2)2Prlmn/J) were obtained from The Jackson Laboratory. All animals
710 were housed in groups of 3 to 5 and fed standard chow diets. The photoperiod was 12 h on:12 h
711 off dark/light cycle. The ambient animal room temperature was 70° F, controlled within ±2° and
712 the room humidity was 50%, controlled within ±5%. Eight- to ten-week-old female K18-hACE2
713 mice were administered indicated doses of S309 or control (anti-WNV hE16) mAb dose by
714 intraperitoneal injection one day before or after intranasal inoculation with 10^4 FFU of BQ.1.1.
715 Weight was recorded daily, and animals were euthanized on day +6 after virus inoculation.
716
717 **Measurement of viral RNA levels**
718 Tissues were weighed and homogenized with zirconia beads in a MagNA Lyser instrument
719 (Roche Life Science) in 1 mL of DMEM medium supplemented with 2% heat-inactivated FBS.
720 Tissue homogenates were clarified by centrifugation at approximately 10,000 × *g* for 5 min and
721 stored at −80 °C. RNA was extracted using the MagMax mirVana Total RNA isolation kit (Thermo
722 Fisher Scientific) on the Kingfisher Flex extraction robot (Thermo Fisher Scientific). RNA was
723 reverse transcribed and amplified using the TaqMan RNA-to-CT 1-Step Kit (Thermo Fisher
724 Scientific). Reverse transcription was carried out at 48 °C for 15 min followed by 2 min at 95 °C.
725 Amplification was accomplished over 50 cycles as follows: 95 °C for 15 s and 60 °C for 1 min.
726 Copies of SARS-CoV-2 *N* gene RNA in samples were determined using a previously published
727 assay[42]. Briefly, a TaqMan assay was designed to target a highly conserved region of the *N* gene
728 (Forward primer: ATGCTGCAATCGTGCTACAA; Reverse primer: GACTGCCGCCTCTGCTC;
729 Probe: /56-FAM/TCAAGGAAC/ZEN/AACATTGCCAA/3IABkFQ/). This region was included in an

730 RNA standard to allow for copy number determination down to 10 copies per reaction. The
731 reaction mixture contained final concentrations of primers and probe of 500 and 100 nM,
732 respectively.
733
734 **Viral plaque assay**
735 VeroE6-TMPRSS2-ACE2 cells were seeded at a density of 1×10^5 cells per well in 24-well tissue
736 culture plates. The following day, medium was removed and replaced with 200 µL of material to
737 be titrated diluted serially in DMEM supplemented with 2% FBS. One hour later, 1 mL of
738 methylcellulose overlay was added. Plates were incubated for 72 h, and then fixed with 4%
739 paraformaldehyde (final concentration) in PBS for 20 min. Plates were stained with 0.05% (w/v)
740 crystal violet in 20% methanol and washed twice with distilled, deionized water.
741
742 **Transient expression of recombinant SARS-CoV-2 protein and flow cytometry.**
743 ExpiCHO-S cells were seeded at 6×10^6 cells/mL in a volume of 5 mL in a 50 mL bioreactor. The
744 following day, cells were transfected with SARS-CoV-2 spike glycoprotein-encoding pcDNA3.1(+)
745 plasmids (BetaCoV/Wuhan-Hu-1/2019, accession number MN908947, Wu-D614; Omicron BA.2,
746 BQ.1.1, XBB.1 and BA.2-E340A generated by overlap PCR mutagenesis of the Wuhan D614
747 plasmid) harboring the Δ19 C-terminal truncation. Spike encoding plasmids were diluted in cold
748 OptiPRO SFM (Life Technologies, 12309-050), mixed with ExpiFectamine CHO Reagent (Life
749 Technologies, A29130) and added to cells. Transfected cells were then incubated at 37°C with
750 8% CO2 with an orbital shaking speed of 250 RPM (orbital diameter of 25 mm) for 24 to 48 h.
751 Transiently transfected ExpiCHO-S cells were harvested and washed twice in wash buffer (PBS
752 2% FBS, 2mM EDTA). Cells were counted and distributed into round bottom 96-well plates
753 (Corning, 3799) and incubated with serial dilutions of mAb starting at 10 µg/mL. Alexa Fluor647-
754 labelled Goat anti-human IgG secondary Ab (Jackson ImmunoResearch, 109–606–098) was
755 prepared at 2 µg/mL and added onto cells after two washing steps. Cells were then washed twice
756 and resuspended in wash buffer for data acquisition at Ze5 cytometer (BioRad).
757
758 **Fc-mediated effector functions (ADCC).**
759 Primary cells were collected from healthy human donors with informed consent and authorization
760 via the Comitato Etico Canton Ticino (Switzerland). ADCC assays were performed using
761 ExpiCHO-S cells transiently transfected with SARS-CoV-2 spike glycoproteins (Wuhan D614,
762 BA.2, BQ.1.1 or XBB.1) as targets. NK cells were isolated from fresh blood of healthy donors
763 using the MACSxpress NK Isolation Kit (Miltenyi Biotec, cat. no. 130-098-185). Target cells were
764 incubated with titrated concentrations of mAbs for 10 min and then with primary human NK cells
765 at an effector to target ratio ranging from 7.75:1 to 9:1. ADCC was measured using the LDH
766 release assay (Cytotoxicity Detection Kit (LDH) (Roche; cat. no. 11644793001) after 4 h
767 incubation at 37°C.
768
769 **Measurement of plasma effector functions.**
770 Antibody-dependent activation of human FcγRIIIa by plasma antibodies was performed with a
771 bioluminescent reporter assay. ExpiCHO-S cells transiently expressing full-length SARS-CoV-2

S from Wuhan-D614, BA.5, BQ.1.1 and XBB.1 (target cells) were incubated with serial dilutions of plasma from immune donors. After a 20-minute incubation, Jurkat reporter cells stably expressing FcγRIIIa V158 and NFAT-driven luciferase gene (effector cells) were added at an effector to target ratio of 6:1 for FcγRIIIa. Signaling was quantified by the luciferase signal produced via activation of the NFAT pathway. Luminescence was measured after 22 hours of incubation at 37˚C with 5% CO_2 with a luminometer using the Bio-Glo-TM Luciferase Assay Reagent according to the manufacturer's instructions (Promega).

Antigen-specific memory B cell repertoire analysis (AMBRA) of secreted IgGs

Replicate cultures of total unfractionated PBMCs obtained from SARS-CoV-2 infected and/or vaccinated individuals were seeded in 96 U-bottom plates (Corning) in RPMI1640 supplemented with 10% fetal calf serum (Hyclone), sodium pyruvate, MEM non-essential amino acids, stable glutamine, 2-mercaptoethanol, Penicillin-Streptomycin, Kanamycin and Transferrin. Memory B cell stimulation and differentiation was induced by adding 2.5 µg/ml R848 (3 M) and 1000 U/ml human recombinant IL-2 at 37 °C and 5% CO_2. After 10 days, the cell culture supernatants were collected for ELISA analysis.

Enzyme-linked immunosorbent assay (ELISA)

Ninety-six half area well-plates (Corning, 3690) were coated overnight at 4 °C with 25 µl of sarbecovirus RBD proteins prepared at 5 µg/ml in PBS pH 7.2. Plates were then blocked with PBS 1% BSA (Sigma-Aldrich, A3059) and subsequently incubated with mAb serial dilutions for 1 h at room temperature. After 4 washing steps with PBS 0.05% Tween 20 (PBS-T) (Sigma-Aldrich, 93773), goat anti-human IgG secondary antibody (Southern Biotech, 2040-04) was added and incubated for 1 h at room temperature. Plates were then washed four times with PBS-T and 4-nitrophenyl phosphate (pNPP, Sigma-Aldrich, 71768) substrate was added. After 30 min incubation, absorbance at 405 nm was measured by a plate reader (Biotek) and data were plotted using Prism GraphPad 9.1.0. To test MBC-derived antibodies, Spectraplate-384 with high protein binding treatment (custom made from Perkin Elmer) were coated overnight at 4°C with 3 µg/ml of RBD (produced in house), SARS-CoV RBD (produced in house), Omicron BA.1, BQ.1.1 and XBB:1 RBDs (produced in house) in PBS pH 7.2 or PBS alone as control. Plates were subsequently blocked with Blocker Casein (1%) in PBS (Thermo Fisher Scientific, 37528) supplemented with 0.05% Tween 20 (Sigma Aldrich, 93773-1KG). The coated plates were incubated with diluted B cell supernatant for 1h at RT. Plates were washed with PBS containing 0.05 % Tween20 (PBS-T), and binding was revealed using secondary goat anti-human IgG-AP (Southern Biotech, 2040-04). After washing, pNPP substrate (Sigma-Aldrich, 71768-25G) was added and plates were read at 405 nm after 1 h or 30 minutes.

Blockade of RBD binding to human ACE2

Memory B cell culture supernatants were diluted in PBS and mixed with SARS-CoV-2 RBD mouse Fc-tagged antigen (Sino Biological, 40592-V05H, final concentration 20 ng/ml) and incubated for 30 min at 37°C. The mix was added for 30 min to ELISA 384-well plates (NUNC, P6366-1CS) pre-coated overnight at 4°C with 4 µg/ml human ACE2 (produced in house) in PBS. Plates were washed with PBS containing 0.05 % Tween20 (PBS-T), and RBD binding was revealed using

815 secondary goat anti-mouse IgG-AP (Southern Biotech, 1032-04). After washing, pNPP substrate
816 (Sigma-Aldrich, 71768-25G) was added and plates were read at 405 nm after 1h.
817

818 **Recombinant protein production for SPR binding assays and AMBRA ELISA**

819 SARS-CoV-2 RBD plasmids encode for residues 328-531 of the spike protein from GenBank
820 NC_045512.2 with an N-terminal signal peptide and a C-terminal 8xHis-AviTag or thrombin
821 cleavage site-8xHis-AviTag. Proteins were expressed in Expi293F cells (Thermo Fisher Scientific)
822 at 37 °C and 8% CO_2. Transfections were performed using the ExpiFectamine 293 Transfection
823 Kit (Thermo Fisher Scientific). Cell culture supernatants were collected four to five days after
824 transfection and supplemented with 10x PBS to a final concentration of 2.5x PBS (342.5 mM
825 NaCl, 6.75 mM KCl and 29.75 mM phosphates). SARS-CoV-2 RBDs were purified by IMAC using
826 Cobalt or Nickel resin followed by buffer exchange into PBS using Amicon centrifugal filters
827 (Milipore Sigma) or by size exclusion chromatography using a Superdex 200 Increase 10/300 GL
828 column (Cytiva). For SPR binding measurements, recombinant ACE2 (residues 19-615 from
829 Uniprot Q9BYF1 with a C-terminal thrombin cleavage site-TwinStrep-10xHis-GGG-tag, and N-
830 terminal signal peptide) was expressed in Expi293F cells at 37°C and 8% CO_2. Transfection was
831 performed using the ExpiFectamine 293 Transfection Kit (Thermo Fisher Scientific). Cell culture
832 supernatant was collected seven days after transfection, supplemented to a final concentration of
833 80 mM Tris-HCl pH 8.0, 100 mM NaCl, and then incubated with BioLock solution (IBA GmbH).
834 ACE2 was purified using a 1 mL StrepTrap HP column (Cytiva) followed by isolation of the
835 monomeric ACE2 by size exclusion chromatography using a Superdex 200 Increase 10/300 GL
836 column (Cytiva) pre-equilibrated in PBS. Recombinant S309 Fab used for SPR binding studies
837 was produced in ExpiCHO-S cells and purified using a Capture Select CH1-XL MiniChrom
838 Column (ThermoFisher), followed by buffer exchange into PBS using a HiPrep 26/10 Desalting
839 Column (Cytiva).
840

841 **Surface plasmon resonance (SPR) assays to measure binding of the S309 Fab to RBDs**

842 Measurements were performed using a Biacore T200 instrument. A CM5 chip with covalently
843 immobilized StrepTactin XT was used for surface capture of Twin-Strep Tag-containing RBDs.
844 Running buffer was HBS-EP+ pH 7.4 (Cytiva) and measurements were performed at 25℃.
845 Experiments were performed with a 3-fold dilution series of monomeric S309 Fab at 300, 100, 33
846 and 11 nM and were run as single-cycle kinetics. Data were double reference-subtracted and fit
847 to a binding model using Biacore Evaluation software. The 1:1 binding model was used to
848 estimate the kinetics parameters. The experiment was performed twice with two biological
849 replicates for each ligand (RBDs). K_D values are reported as the average of two replicates with
850 the corresponding standard deviation.
851

852 **Cell-cell fusion assay**

853 Cell-cell fusion assays using a split GFP system was conducted as previously described. In brief,
854 VeroE6-TMPRSS2-GFP_{11} cells were split into 96-well, glass bottom, black walled plates (CellVis)
855 at a density of 36,000 cells per well. BHK-21-GFP_{1-10} cells were split into 6-well plates at a density
856 of 1 x 10^6 cells per well. The following day, the growth media was removed and replaced with
857 DMEM containing 10% FBS and 1% PS and the cells were transfected with 4 µg of S protein

using Lipofectamine 2000. Twenty-four hours after transfection, BHK-21-GFP_{1-10} expressing the S protein were washed three times using FluoroBrite DMEM (Thermo Fisher) and detached using an enzyme-free cell dissociation buffer (Gibco). The VeroE6-TMPRSS2-GFP_{11} were washed three times with FluoroBrite DMEM and 9,000 BHK-21-GFP_{1-10} cells were plated on top of the VeroE6-TMPRSS2-GFP_{11} cells. The cells were incubated at 37°C and 5% CO_2 in a Cytation 7 plate Imager (Biotek) and both brightfield and GFP images were collected every 30 minutes for 18 hours. Fusogenicity was assessed by measuring the area showing GFP fluorescence for each image using Gen5 Image Prime v3.11 software.

To measure surface expression of the variant SARS-CoV-2 S protein, 1 x 10^6 transiently transfected BHK-21-GFP_{1-10} cells were collected by centrifugation at 1,000 x g for 5 min. The cells were washed once with PBS and fixed with 2% paraformaldehyde. The cells were washed twice with flow staining buffer (1% BSA, 1 mM EDTA, 0.1% NaN_3 in PBS) and labeled with 250 µg/mL of S2L20, an NTD-directed antibody that recognizes all currently and previously circulating SARS-CoV-2 variants, for 45 minutes. The cells were washed three times with flow staining buffer and labeled with a PE-conjugated anti-Human IgG Fc antibody (Thermo Fisher) for 30 mins. The cells were washed an additional three times and resuspended in flow staining buffer. The labeled cells were analyzed using a BD FACSymphony A3. ells were gated on singleton events and a total of 10,000 singleton events were collected for each sample. The fraction of S-positive cells was determined in FlowJo 10.8.1 by gating singleton events for the mock transfected cells on PE intensity.

Flow cytometry analysis of SARS-CoV-2 RBD-reactive MBCs

RBD-streptavidin tetramers conjugated to fluorophores were generated by incubating biotinylated Wu, BA.1, BA.2, BA.4/5, or BQ.1.1 with streptavidin at a 4:1 molar ratio for 30 mins at 4°C. Excess free biotin was then added to the reaction to bind any unconjugated sites in the streptavidin tetramers. The RBD-streptavidin tetramers were washed once with PBS and concentrated with a 30 kDa centrifugal concentrator (Amicon). An additional streptavidin tetramer conjugated to biotin only was generated and included in the staining.

Approximately 5 to 15 million PMBCs were collected 5-72 days post-vaccination for individuals who received either the Wu monovalent mRNA booster or Wu/BA.5 bivalent mRNA booster. The cells were collected by centrifugation at 1,000 x g for 5 mins at 4°C and washed twice with PBS. The cells were then stained with Zombie Aqua dye (Biolegend; diluted 1:100 in PBS) for 30 mins at room temperature after which the cells were washed twice with FACS staining buffer (0.1% BSA, 0.1% NaN_3 in PBS). The cells were then stained with antibodies for CD20-PECy7 (BD), CD3-Alexa eFluor780 (ThermoFisher), CD8-Alexa eFluor780 (ThermoFisher), CD14-Alexa eFluor780 (ThermoFisher), CD16-Alexa eFluor780 (ThermoFisher), IgM-Alexa Fluor647 (BioLegend), IgD-Alexa Fluor647 (BioLegend), and CD38-Brilliant Violet 785 (BioLegend), all diluted 1:200 in Brilliant Stain Buffer (BD), along with the RBD-streptavidin tetramers for 30 mins at 4°C. The cells were washed three times, resuspended in FACS staining buffer, and passed through a 35 µm filter. The cells were examined using a BD FACSAria III and FACSDiva for acquisition and FlowJo 10.8.1 for analysis. Single live $CD20^+/CD3^-/CD8^-/CD14^-/CD16^-/IgM^{lo}/IgD^{lo}/CD38^{lo}/RBD^+$ cells were sorted based on reactivity to the Omicron and Wu RBDs into RNAlater and stored at -80°C.

CryoEM sample preparation, data collection and data processing

CryoEM grids of BQ.1.1 RBD-ACE2-S309 or XBB.1 RBD-ACE2-S309 complex were prepared fresh after SEC purification. For BQ.1.1 RBD-ACE2-S309 complex, three microliters of 0.25 mg/ml BQ.1.1 RBD-ACE2-S309 were loaded onto freshly glow discharged R 2/2 UltrAuFoil grids, prior to plunge freezing using a vitrobot MarkIV (ThermoFisher Scientific) with a blot force of 0 and 6 sec blot time at 100 % humidity and 22°C. Data were acquired using an FEI Titan Krios transmission electron microscope operated at 300 kV and equipped with a Gatan K3 direct detector and Gatan Quantum GIF energy filter, operated in zero-loss mode with a slit width of 20 eV. For BQ.1.1 RBD-ACE2-S309 data set, automated data collection was carried out using Leginon at a nominal magnification of 105,000x with a pixel size of 0.843 Å and stage tilt angle of 30˚. 6,487 micrographs were collected with a defocus range comprised between -0.5 and -2.5 µm. For XBB.1 RBD-ACE2-S309 complex, samples were prepared using the Vitrobot Mark IV (Thermo Fisher Scientific) with R 2/2 UltrAuFoil grids and with a Chameleon (SPT Labtech) with self-wicking nanowire Cu R1.2/0.8 holey carbon grids. For XBB.1 RBD-ACE2-S309 data set, 6,355 micrographs from UltrAuFoil grids and 2,889 micrographs from chameleon grids were collected with a defocus range comprised between -0.2 and -3 µm. The dose rate was adjusted to 15 counts/pixel/s, and each movie was acquired in super-resolution mode fractionated in 75 frames of 40 ms. Movie frame alignment, estimation of the microscope contrast-transfer function parameters, particle picking, and extraction were carried out using Warp.

Two rounds of reference-free 2D classification were performed using cryoSPARC to select well-defined particle images. These selected particles were subjected to two rounds of 3D classification with 50 iterations each (angular sampling 7.5˚ for 25 iterations and 1.8˚ with local search for 25 iterations) using Relion with an initial model generated with ab-initio reconstruction in cryoSPARC. 3D refinements were carried out using non-uniform refinement along with per-particle defocus refinement in CryoSPARC. Selected particle images were subjected to the Bayesian polishing procedure implemented in Relion3.0 before performing another round of non-uniform refinement in cryoSPARC followed by per-particle defocus refinement and again non-uniform refinement. To further improve the density of the BQ.1.1 RBD and XBB.1 RBD, the particles were subjected to focus 3D classification without refining angles and shifts using a soft mask encompassing the ACE2, RBD and S309 variable domains using a tau value of 60 in Relion. Particles belonging to classes with the best resolved local density were selected and subjected to non-uniform refinement using cryoSPARC. Local resolution estimation, filtering, and sharpening were carried out using CryoSPARC. Reported resolutions are based on the gold-standard Fourier shell correlation (FSC) of 0.143 criterion and Fourier shell correlation curves were corrected for the effects of soft masking by high-resolution noise substitution.

Model building and refinement

UCSF Chimera and Coot were used to fit atomic models into the cryoEM maps. Spike RBD domain, ACE2, S309 Fab models were refined and relaxed using Rosetta using sharpened and unsharpened maps.

Statistical Analysis

All statistical tests were performed as described in the indicated figure legends using Prism v9.0. The number of independent experiments performed are indicated in the relevant figure legends.

Data Availability

All datasets generated and information presented in the study are available from the corresponding authors on reasonable request. Materials generated in this study can be available on request and may require a material transfer agreement.

Acknowledgements

We would like to thank Abigail E. Powell, Yvonne M. DaCosta, John M. Errico and Ashley Lin for assistance with protein production. This study was supported by the National Institute of Allergy and Infectious Diseases (DP1AI158186 and HHSN272201700059C to D.V.), the National Institute of Health Cellular and Molecular Biology Training Grant (T32GM007270 to A.A.), a Pew Biomedical Scholars Award (D.V.), an Investigators in the Pathogenesis of Infectious Disease Awards from the Burroughs Wellcome Fund (D.V.), Fast Grants (D.V.), the University of Washington Arnold and Mabel Beckman cryoEM center and the National Institute of Health grant S10OD032290 (to D.V.). D.V. is an Investigator of the Howard Hughes Medical Institute. O.G. is funded by the Swiss Kidney Foundation. We acknowledge the Research Council of Cantonal Hospital Aarau for the financial support (to M.J.K.).

Author Contributions

A.A, L.P., D.C. and D.V. designed the experiments; A.A, K.S., M.B., H.D., J.B., C.S.F., F.M., D.P., C.Sa., M.G., R.A., D.J., C.M., E.D., C.S, C.Y., A.R. and S.Su. performed binding, neutralization assays, biolayer interferometry and surface plasmon resonance binding measurements. L.A.P, G.Sc. and D.V. supervised in vitro neutralization assays. E.C. and K.C. designed and performed mutagenesis for the spike mutant expression plasmids. G.L., G.Le., B.G., L.V. and M.A.S. performed experiments to measure effector functions; A.A., C.S.F., M.B., F.M., J.B. and L.P performed memory B cell repertoire analysis. A.A. carried out membrane fusion and protease inhibition experiments. O.G., A.C., P.F., N.F., M.D., O.G., A.C., P.F., A.F.P., M.B., C.G., S.Z., L.B., M.J.K., J.K.L., N.F., and H.C. contributed to the recruitment of donors and collection of plasma samples. J.B.C., S.S. and B.W. performed mouse experiments and viral burden analyses. Y.J.P. carried out cryoEM specimen preparation, data collection and processing. Y.J.P. and D.V. built and refined the atomic models. C.S. purified recombinant glycoproteins. A.A, L.P., G.S., A.L., M.S.D., D.C. and D.V. analyzed the data and wrote the manuscript with input from all authors; M.S.D, D.C., and D.V. supervised the project.

Competing Interests

L.P., M.B., B.G., H.D., J.B., C.S.F., F.M., M.D., D.P., L.V., C.Sa., M.G., G.L., G.Le., C.M., E.D., A,R., R.A., D.J., S.S., K.C., E.C., G.Sc., N.C., M.A.S., L.A.P., G.S., A.L. and D.C. are employees of and may hold shares in Vir Biotechnology Inc. L.A.P. is a former employee and shareholder of Regeneron Pharmaceuticals and is member of the Scientific Advisory Board AI-driven Structure-enabled Antiviral Platform (ASAP). Regeneron provided no funding for this work. M.S.D. is a

consultant for Inbios, Vir Biotechnology, Senda Biosciences, Generate Biomedicines, Moderna, and Immunome. The Diamond laboratory has received unrelated funding support in sponsored research agreements from Moderna and Emergent BioSolutions. The remaining authors declare that the research was conducted in the absence of any commercial or financial relationships that could be construed as a potential conflict of interest.

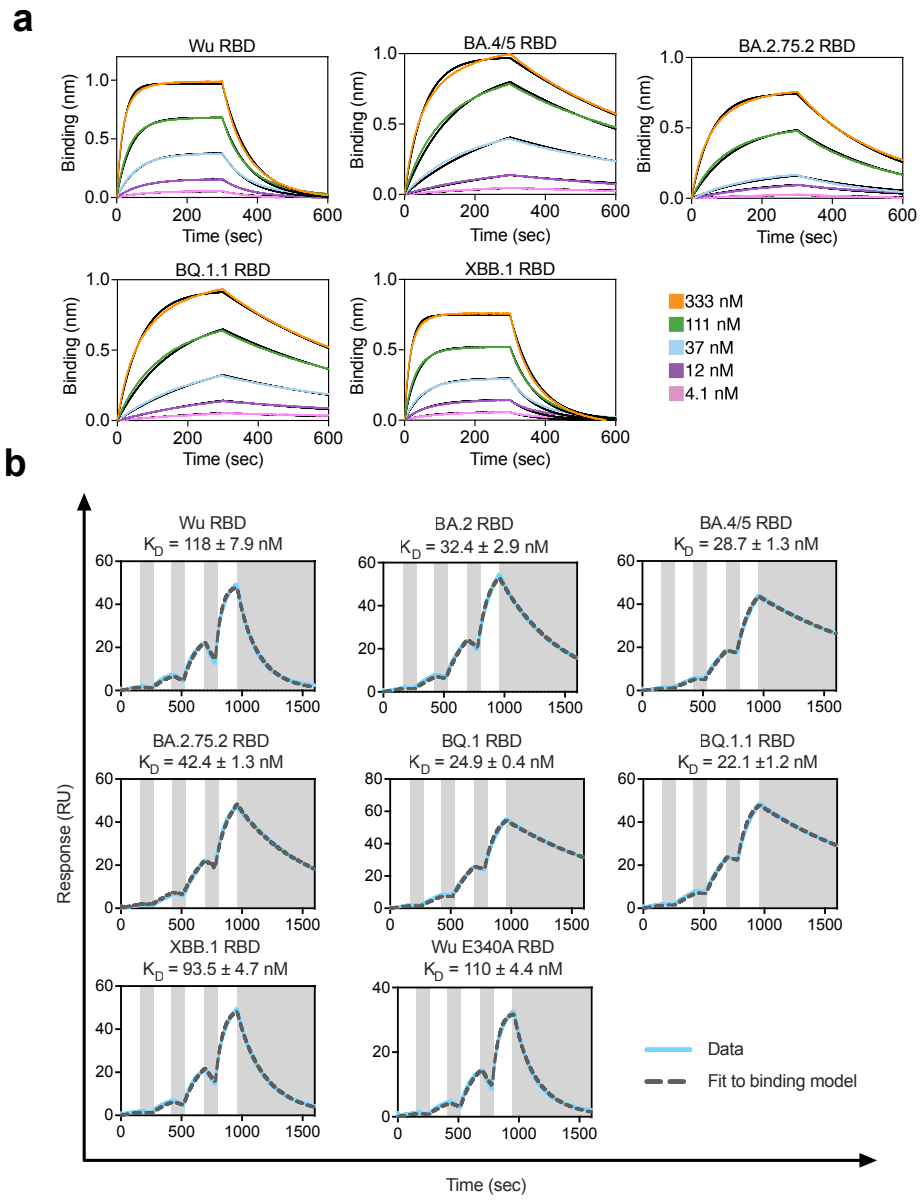

Extended Data Fig. 1. Evaluation of human ACE2 binding to SARS-CoV-2 variant RBDs. a, Biolayer interferometry binding curves obtained for monomeric human ACE2 binding to biotinylated Wu**,** BA.4/5, BA.2.75.2, BQ.1.1, or XBB.1 RBDs immobilized on the surface of streptavidin biosensors. Kinetic rate constants and affinities are shown in **Supplementary Table 1**. Fits are shown as solid black lines. **b**, SPR sensorgrams of monomeric human ACE2 binding to the Wu (Wild-type, WT), BA.2, BA.2.75.2, BA.5, BQ.1, BQ.1.1, XBB.1 and Wu E340A RBDs immobilized at the surface of a SPR chip coated with anti-Avi polyclonal antibody. Experiments were performed with serial dilutions of Fabs and run as single-cycle kinetics. Gray blocks denote the dissociation phase. Fits are shown as dashed grey lines. Kinetic rate constants and affinities are shown in **Supplementary Table 2**.

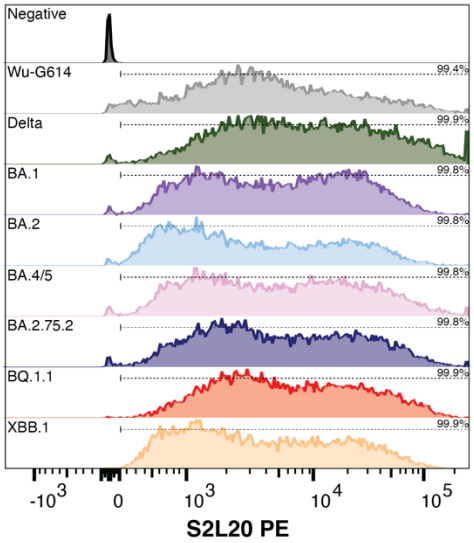

Extended Data Fig. 2. Membrane fusion assay. Quantification of SARS-CoV-2 S surface expression by flow cytometry for BHK-21 GFP_{1-10} cells transfected with Wu-G614, Delta, BA.1, BA.2, BA.4/5, BA.2.75.2, BQ.1.1, or XBB.1 S proteins using the NTD-directed antibody S2L20[24,37]. The y-axis is present as a modal scale scaled to maximum singleton events for that plot. The percentage of S-positive cells is based on the PE intensity for mock transfected (negative) cells and represented by the dashed line above each plot.

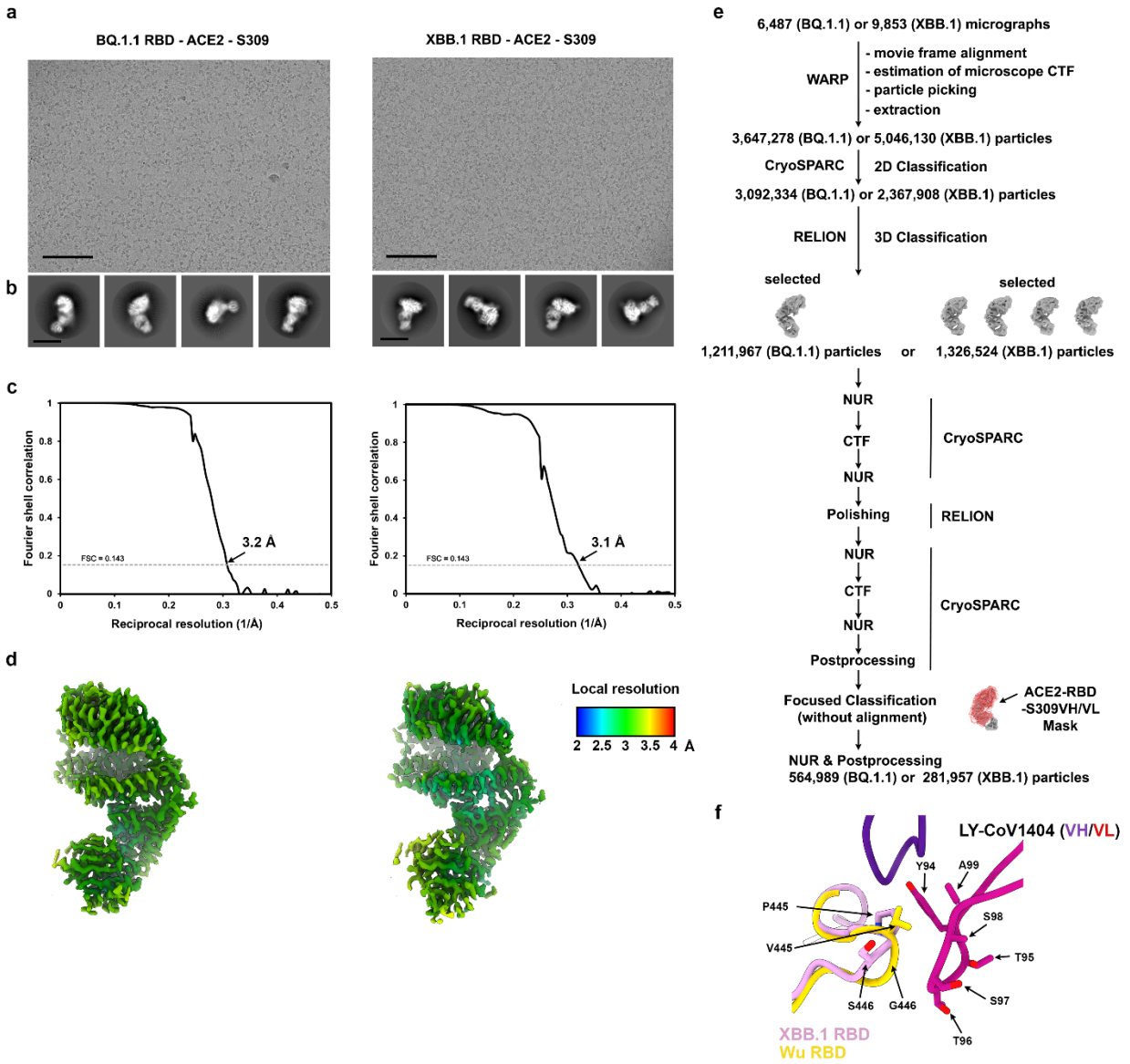

Extended Data Fig. 3. CryoEM data processing of the BQ.1.1 or the XBB.1 RBDs bound to ACE2 and S309. a-b, Representative electron micrograph (a) and 2D class averages (b) of the BQ.1.1 RBD (left) or the XBB.1 RBD (right) bound to the human ACE2 ectodomain and the S309 Fab fragment embedded in vitreous ice. The scale bar represents 100nm (a) or 100 Å (b). **c-d,** Gold-standard Fourier shell correlation curves (c) and local resolution maps calculated using cryoSPARC (d) for the 3D reconstructions of the BQ.1.1 RBD (left) or the XBB.1 RBD (right) bound to the human ACE2 ectodomain and the S309 Fab fragment. The 0.143 cutoff is indicated by a horizontal dashed line. **e,** Data processing flowchart. CTF: contrast transfer function; NUR: non-uniform refinement. **f,** Superimposition of the LYCoV1404-bound Wu RBD (gold, PDB 7MMO) crystal structure to the ACE2- and S309-bound XBB.1 RBD (pink) cryoEM structure (S309 and ACE2 are not shown for clarity).

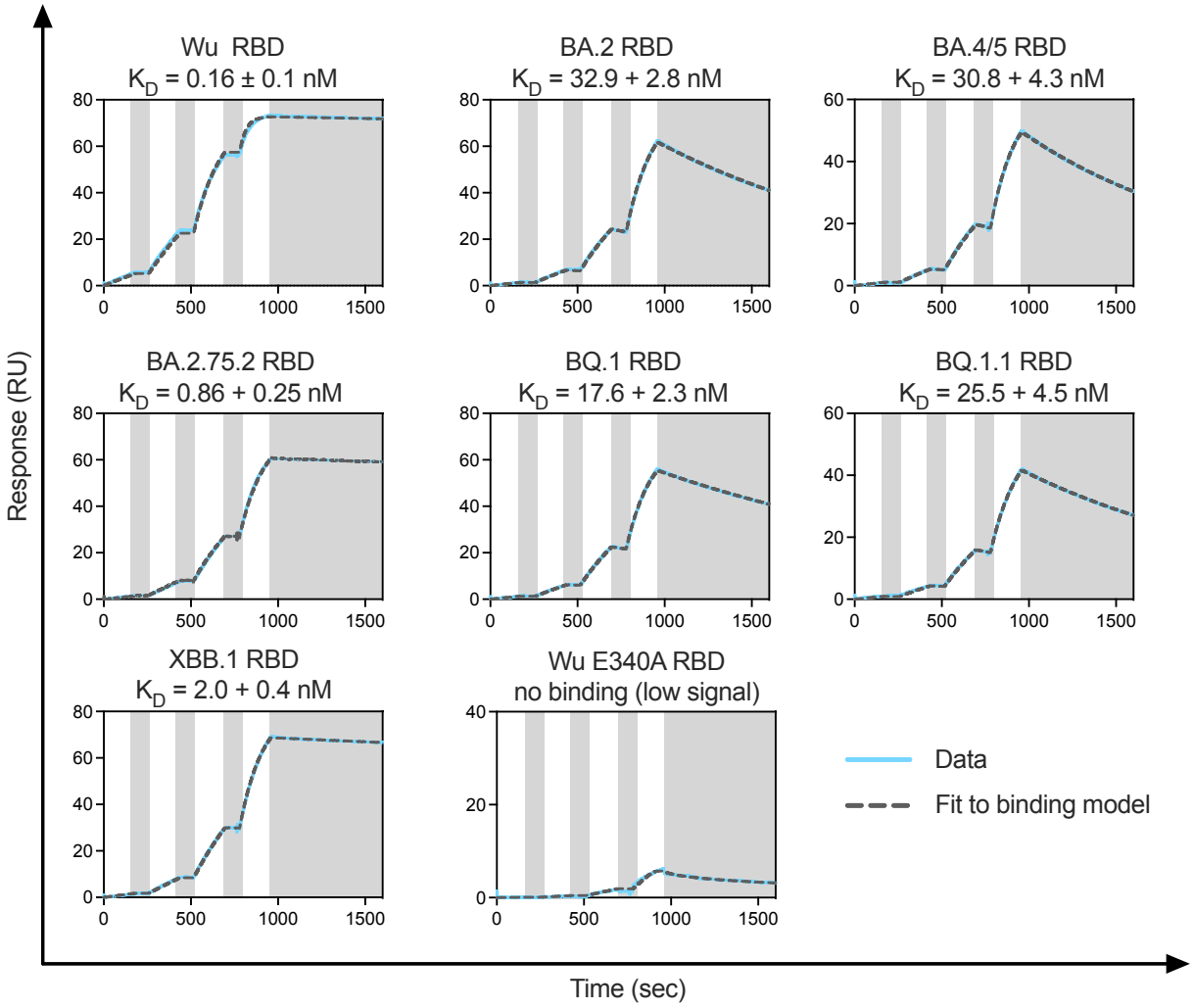

Extended Data Fig. 4. Cross-reactivity of S309 with SARS-CoV-2 variant RBDs. Representative sensograms of S309 Fab binding to the SARS-CoV-2 Wu, BA.2, BA.2.75.2, BA.5, BQ.1, BQ.1.1, XBB.1 and Wu E340A RBDs immobilized at the surface of a SPR chip coated with anti-Avi polyclonal antibody. Experiments were performed with serial dilutions of Fabs and were run as single-cycle kinetics. Gray blocks denote the dissociation phase. Fits are shown as dashed grey lines. Kinetic rate constants and affinities are shown in **Supplementary Table 4**.

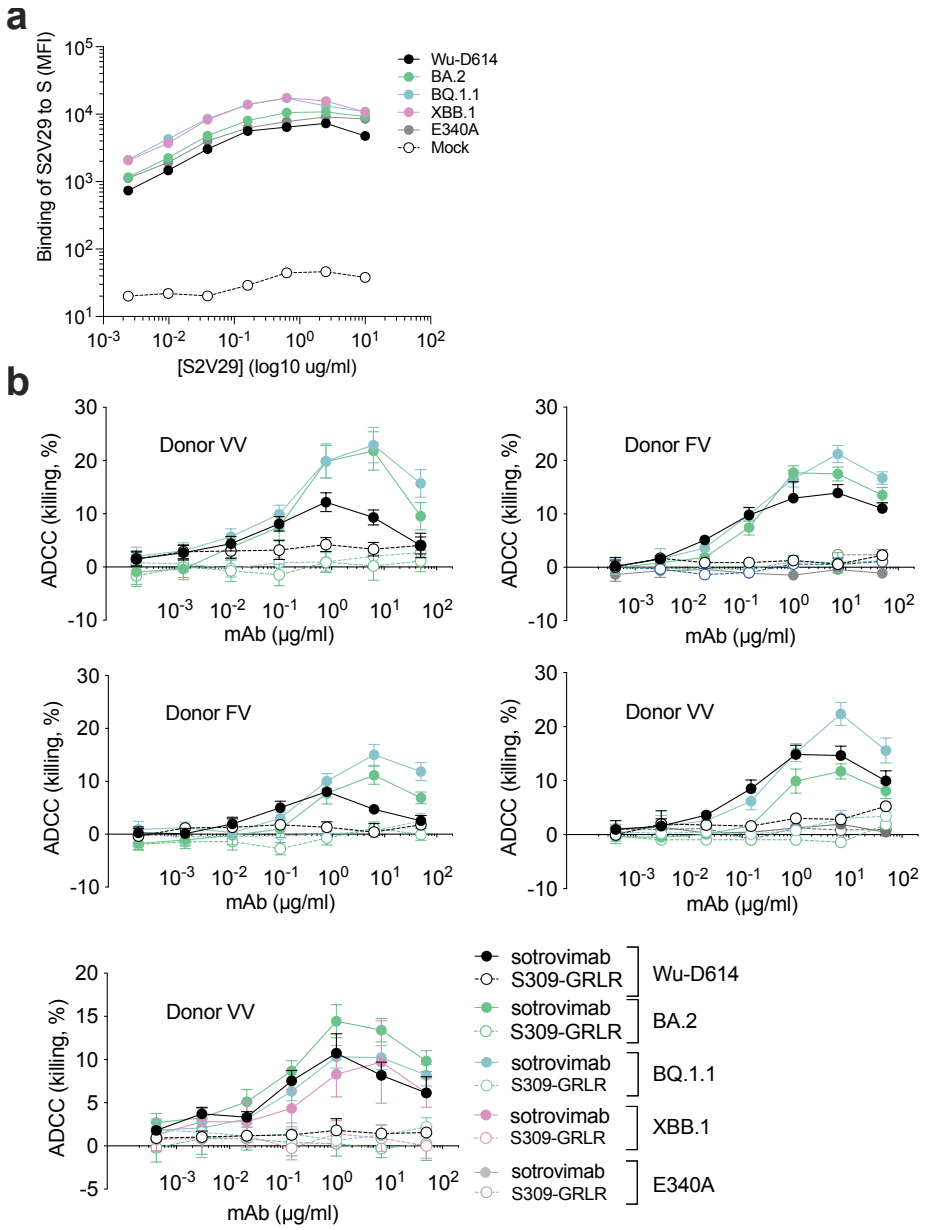

Extended Data Fig. 5. Sotrovimab-mediated ADCC using primary human NK cells. a, Binding of the S2V29 monoclonal antibody to SARS-CoV-2 S variants expressed at the surface of ExpiCHO-S cells as measured by flow cytometry. S2V29 is a mAb that retains potent and equal neutralizing activity against Wu-D614, BA.2, BQ.1.1, XBB.1 and E340A VSV pseudoviruses. **b,** ExpiCHO-S cells transiently transfected with expression plasmids encoding Wuhan D614, BA.2, BQ.1.1, XBB.1 and BA.2-E340A S proteins were incubated with the indicated concentrations of sotrovimab or S309-GRLR and mixed with NK cells isolated from healthy donors in a range from 7.75:1 to 9:1 (effector:target). Target cell lysis was determined by a lactate dehydrogenase release assay. Data are presented as mean values +/– standard deviations (SD) from duplicates. Each panel is an individual representative donor. Donors FV, heterozygous for F158 and V158 FcγRIIIa; VV, homozygous for V158.

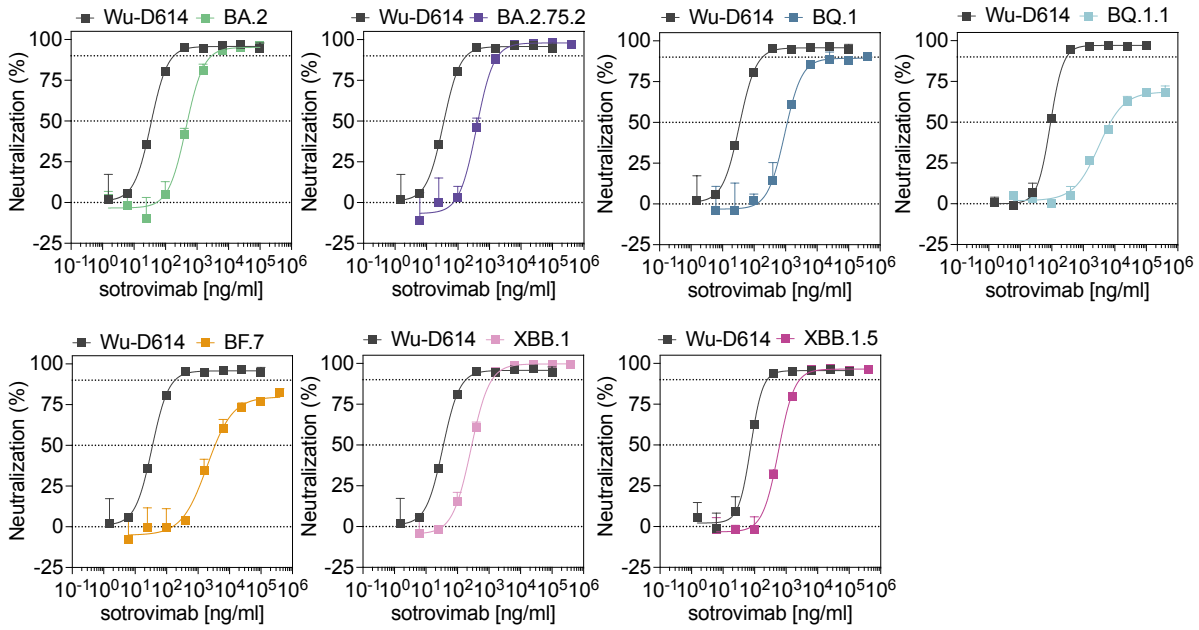

Extended Data Fig. 6. Sotrovimab neutralization of SARS-CoV-2 Omicron variants. Sotrovimab-mediated neutralization of Wu-D614, BA.2, BA.2.75.2, BQ.1, BQ.1.1, BF.7, XBB.1 and XBB.1.5 S VSV pseudoviruses using VeroE6 as target cells. Dose-response curves of one representative experiment out of at least 5 experiments are shown.

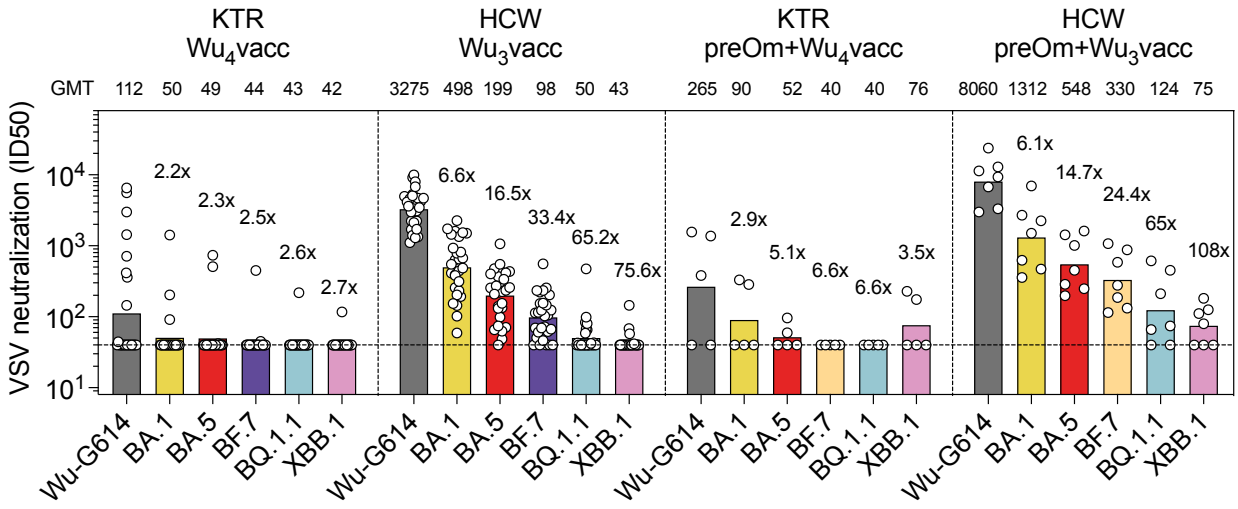

Extended Data Fig. 7 Vaccine-elicited plasma neutralizing antibodies against emerging Omicron variants in kidney transplant recipients. Neutralization of SARS-CoV-2 pseudotyped VSV carrying Wu-G614, Omicron BA.1, BA.5, BF.7, BQ.1.1 and XBB.1 by serum samples from kidney transplant recipients (KTR) or healthcare workers (HCW) collected 2-4 months after receiving 4 (Wu_4vacc) or 3 doses (Wu_3vacc) of monovalent Wu vaccine, respectively. Shown are ID50 values from n = 2 technical replicates. Bars and values on top represent geometric mean ID50 titers (GMT). Fold-loss of neutralization against Omicron variants as compared to Wu-G614 is shown above each corresponding bar. Horizontal dashed lines indicate the lowest limit of detectable neutralization in these assays (ID50 = 40). Cohort demographics are summarized in **Supplementary Table 6**.

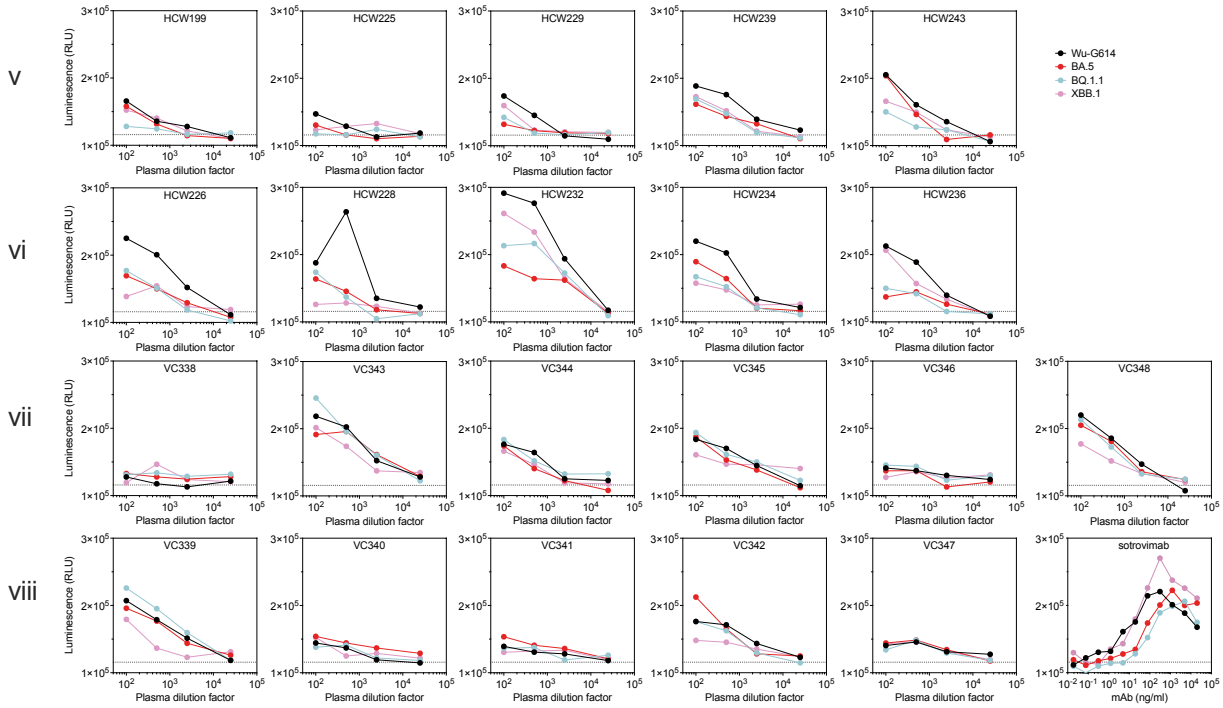

Extended Data Fig 8. Analysis of individual plasma samples activating FcγRIIIa. Activation of high-affinity (V158) FcγRIIIa measured using Jurkat reporter cells and Wu-G614, BA.5, BQ.1.1 and XBB.1 SARS-CoV-2 S glycoprotein-expressing ExpiCHO as target cells. Luminescence (RLU) values from one experiment are shown with plasma samples from cohorts v-viii (n=5 donors for cohort v, n=5 for cohort vi, n=6 for cohort vii and n=5 for cohort viii) and compared to sotrovimab. Horizontal dotted line indicates the lowest limit of detectable activation (RLU = 115,737).

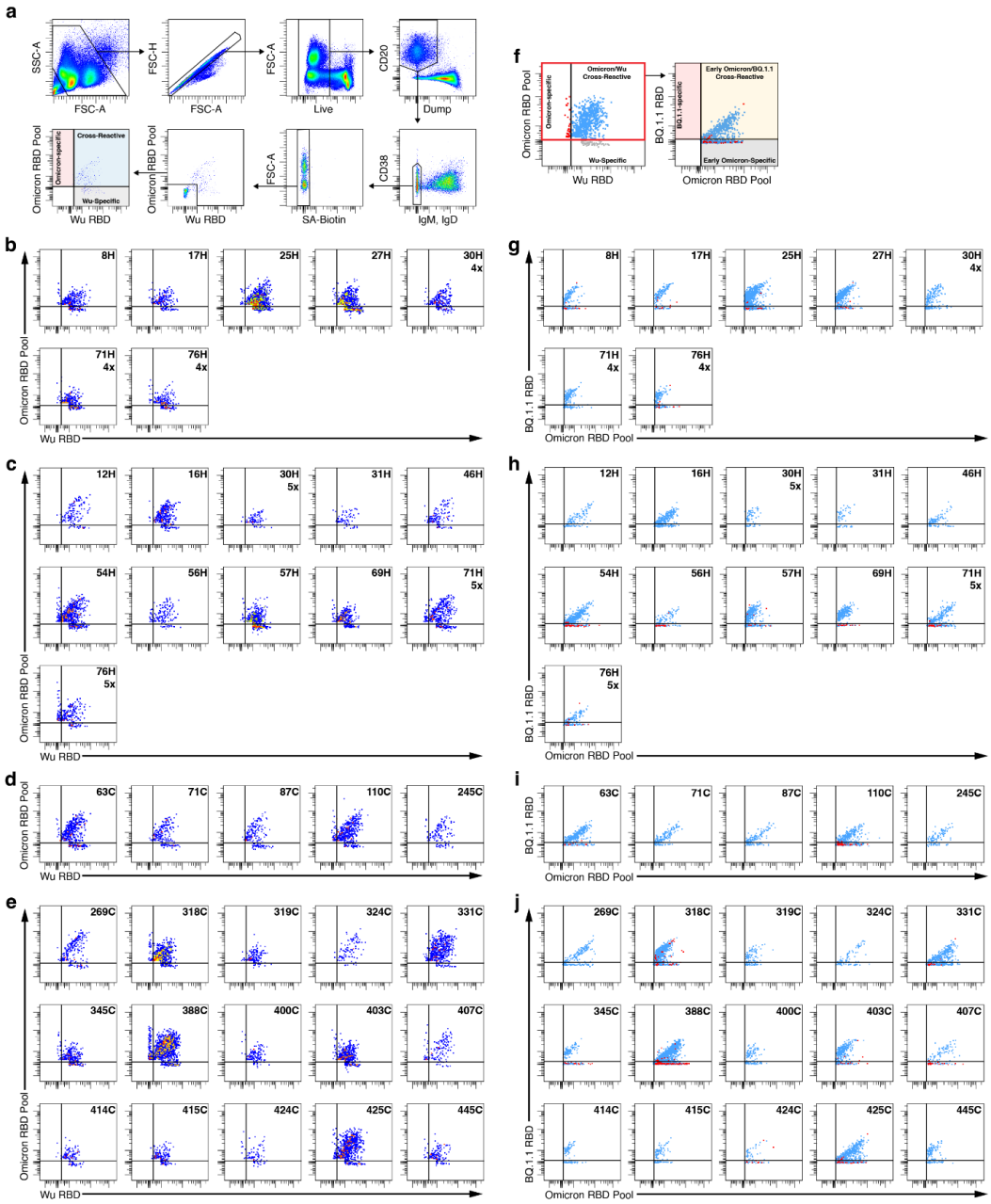

Extended Data Fig. 9 MBC analysis by flow cytometry. a, Gating strategy to identify Omicron (BA.1/BA.2/BA.5) pool RBD- and Wu RBD-recognizing MBCs. Dump includes markers for CD3, CD8, CD14, and CD16. Gating for RBD-positive memory B cells was based on staining of PBMCs from healthy donors collected in 2019 prior to the SARS-CoV-2 pandemic. Individual plots showing Omicron (BA.1/BA.2/BA.5) pool RBD- and Wu RBD-positive MBCs for Wu_4 vaccinated (b), Wu/BA.5 bivalent vaccinated (c), pre-Omicron infected-Wu/BA.5 bivalent vaccinated (d), and Omicron BT-Wu/BA.5 bivalent vaccinated individuals (e). **f**, Gating strategy to determine whether (BA.1, BA.2, and BA.4/5) pool RBD-positive MBCs recognize the BQ.1.1 RBD. Individual plots showing Omicron (BA.1, BA.2, and BA.4/5) RBD pool and BQ.1.1 RBD-recognizing memory B cells for Wu4 vaccinated (g), Wu/BA.5 bivalent vaccinated (h), pre-Omicron infected-Wu/BA.5 bivalent vaccinated (i), and Omicron BT-Wu/BA.5 bivalent vaccinated individuals (j).

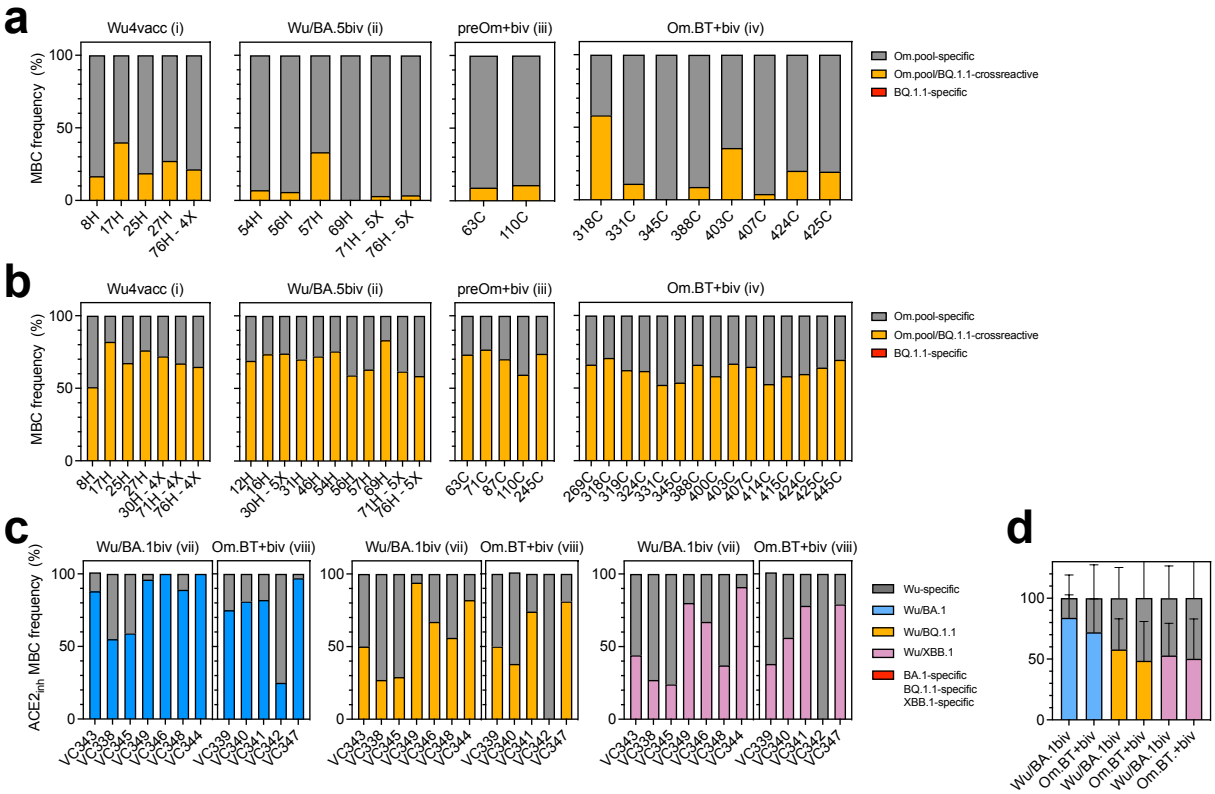

Extended Data Figure 10. Subanalysis of cross-reactivity of vaccine-elicited MBCs. a-c, Analysis of cross-reactivity with BQ.1.1 of Omicron-specific (a) and Wu/Omicron-cross-reactive (b). Om.pool, MBCs reactive to Omicron BA.1, BA.2 or BA.5 RBDs in cohorts i-iv. **c, d,** Individual (c) and mean±sd (d) frequencies of Wu-G614-specific (grey), Omicron-specific (red) and Wu/Omicron-cross-reactive (blue for BA.1, yellow for BQ.1.1 and purple for XBB.1) MBCs showing inhibition of binding of ACE2 to RBD from donors of cohorts vii and viii.

1106 **Supplementary Table 1. Kinetics of monomeric human ACE2 binding to immobilized**
1107 **SARS-CoV-2 variant RBDs as measured by biolayer interferometry.**

	K_D (nM)	k_{on} ($M^{-1}s^{-1}$)	k_{off}(s^{-1})
Wuhan-Hu-1	101.1 ± 7.3	1.30×10^{5}	1.31×10^{-2}
BA.4/5	12.8 ± 2.2	1.45×10^{5}	1.82×10^{-3}
BA.2.75.2	26.2 ± 1.7	1.35×10^{5}	3.52×10^{-3}
BQ.1.1	13.7 ± 1.4	1.39×10^{5}	1.89×10^{-3}
XBB.1	88.4 ± 11.9	1.47×10^{5}	1.29×10^{-2}

1108 Values are presented as mean ± standard deviation

1109 **Supplementary Table 2. Kinetics of monomeric human ACE2 binding to immobilized**
1110 **SARS-CoV-2 variant RBDs as measured by Surface Plasmon Resonance.**

RBD	average KD (nM)	stdev (KD) (nM)	averaged ka (1/Ms)	stdev(ka) (1/Ms)	averaged kd (1/s)	stdev(kd) (1/s)	Number of replicates
Wu-Hu-WT	117.93	7.86	6.09E+04	6.65E+03	6.09E+04	6.65E+03	3
Wu-Hu E340A	110.25	4.35	5.42E+04	1.36E+04	5.95E-03	1.26E-03	3
BA.2	32.40	2.90	2.27E+04	1.92E+03	7.34E-04	8.47E-05	3
BA.4/5	28.72	1.28	2.69E+04	4.17E+02	7.73E-04	2.26E-05	2

1111 Averaged binding affinity (KD in nM unit), corresponding standard deviation, and number of replicates for
1112 each RBD-ACE2 pair. N/A: standard deviation calculation not applicable because only one replicate
1113 produces data within the instrument's limit. NB: no binding; N/A: not applicable.

1114 **Supplementary Table 3. CryoEM data collection and refinement statistics.**

	SARS-CoV-2 BQ.1.1 RBD - ACE2-S309 PDB EMD	SARS-CoV-2 XBB.1 RBD - ACE2-S309 PDB EMD
Data collection and processing		
Magnification	105,000	105,000
Voltage (kV)	300	300
Electron exposure (e^{-}/Å^2)	60	60
Defocus range (μm)	-0.5 - -2.5	-0.2 - -3.0
Pixel size (Å)	0.843	0.843
Symmetry imposed	C1	C1
Final particle images (no.)	564,989	281,957
Map resolution (Å)	3.2	3.1
FSC threshold	0.143	0.143
Map sharpening *B* factor (Å^2)	-150	-120
Validation		
MolProbity score	0.95	1.51
Clashscore	1.07	5.94
Poor rotamers (%)	0.46	0.48
Ramachandran plot		
Favored (%)	97.26	96.87
Allowed (%)	2.64	2.71
Disallowed (%)	0.1	0.42

1115

1116 **Supplementary Table 4. Kinetics of S309 Fab binding to immobilized SARS-CoV-2 variant**
1117 **RBDs as measured by Surface Plasmon Resonance.**

RBD	average K_D (nM)	stdev(K_D) (nM)	averaged kon (1/Ms)	stdev(kon) (1/Ms)	averaged koff (1/s)	stdev(koff) (1/s)	Number of replicates
Wuhan-Hu-WT	0.16	0.09	9.12E+04	9.86E+03	1.41E-05	7.06E-06	7
Wuhan-Hu E340A	NB	N/A	NB	N/A	NB	N/A	3
BA.1	10.88	2.51	2.29E+04	2.49E+03	2.45E-04	3.23E-05	4
BA.2	32.88	2.79	2.16E+04	2.01E+03	7.05E-04	5.25E-05	8
BA.4/5	30.82	4.33	2.49E+04	1.97E+03	7.60E-04	7.08E-05	14
BA.2.75.2	0.86	0.25	2.87E+04	3.14E+03	2.43E-05	5.52E-06	6
BQ.1	17.63	2.31	2.51E+04	1.39E+03	4.40E-04	3.60E-05	5
BQ.1.1	25.49	4.46	2.34E+04	1.79E+03	5.92E-04	6.60E-05	3
XBB.1	1.96	0.44	2.73E+04	1.60E+03	5.32E-05	1.06E-05	3

1118 Averaged binding affinity (K_D in nM unit), corresponding standard deviation, and number of replicates for each RBD-
1119 S309 Fab pair. N/A: standard deviation calculation not applicable because only one replicate produces data within the
1120 instrument's limit. NB: no binding; N/A: not applicable.
1121

1122 **Supplementary Table 5. Donors' demographics.**

Donor ID	Gender	Vaccine doses	COVID diagnosis	SARS-CoV-2 variant	D sample-vacc (days)	Cohort
15H	M	4	no	/	5	Wu_4vacc
17H	M	4	no	/	21	Wu_4vacc
25H	M	4	no	/	16	Wu_4vacc
27H	M	4	no	/	42	Wu_4vacc
30H - 4X	F	4	no	/	17	Wu_4vacc
46H	M	4	no	/	15	Wu_4vacc
71H - 4x	F	4	no	/	48	Wu_4vacc
76H - 4x	F	4	no	/	13	Wu_4vacc
8H	M	4	no	/	72	Wu_4vacc
12H	F	4	no	/	34	Wu/BA.5biv
16H	F	4	no	/	33	Wu/BA.5biv
17H	M	5	no	/	18	Wu/BA.5biv
29H	M	5	no	/	37	Wu/BA.5biv
30H - 5x	F	5	no	/	30	Wu/BA.5biv
31H*	F	3	no	/	54	Wu/BA.5biv
46H	M	5	no	/	16	Wu/BA.5biv
51H	F	4	no	/	33	Wu/BA.5biv
54H	F	4	no	/	27	Wu/BA.5biv
56H	M	4	no	/	28	Wu/BA.5biv
57H	M	5	no	/	46	Wu/BA.5biv
69H	F	5	no	/	42	Wu/BA.5biv
71H - 5x	F	5	no	/	20	Wu/BA.5biv
76H - 5x	F	5	no	/	60	Wu/BA.5biv
110C	M	5	yes	WA-1	38	preOm+biv
245C	F	4	yes	WA-1	25	preOm+biv
63C	F	4	yes	WA-1	33	preOm+biv
71C	F	5	yes	WA-1	28	preOm+biv
87C	M	5	yes	WA-1	30	preOm+biv
269C	M	4	yes	Gamma/P.1 & Om. BA.1	30	Om.BT+biv
318C	F	4	yes	Omicron	42	Om.BT+biv
319C	M	4	yes	Omicron	28	Om.BT+biv
324C	F	4	yes	Omicron	32	Om.BT+biv
331C	M	5	yes	Omicron	33	Om.BT+biv
345C	M	4	yes	Omicron	28	Om.BT+biv
388C	M	4	yes	Omicron BA.5	45	Om.BT+biv
400C	F	4	yes	Omicron BA.2	22	Om.BT+biv
403C	F	4	yes	Omicron BA.2.12.1	33	Om.BT+biv
407C	F	4	yes	Omicron BA.2	34	Om.BT+biv
414C	M	4	yes	Omicron BA.4	51	Om.BT+biv
415C	F	4	yes	Omicron BA.2	30	Om.BT+biv
424C	F	4	yes	Omicron BA.2.12.1	29	Om.BT+biv
425C	M	4	yes	Omicron BA.2.12.1	31	Om.BT+biv
428C	F	4	yes	Omicron BA.5	13	Om.BT+biv
445C	F	4	yes	Omicron BA.5	36	Om.BT+biv
HCW199	M	3	no	/	18	Wu_3vacc
HCW225	F	3	no	/	25	Wu_3vacc
HCW229	F	3	no	/	20	Wu_3vacc
HCW239	F	3	no	/	26	Wu_3vacc
HCW243	F	3	no	/	27	Wu_3vacc
HCW198	M	3	yes	pre Omicron	18	preOm+vacc
HCW200	F	3	yes	pre Omicron	13	preOm+vacc
HCW202	M	3	yes	pre Omicron	13	preOm+vacc
HCW221	F	3	yes	pre Omicron	20	preOm+vacc
HCW224	F	3	yes	pre Omicron	18	preOm+vacc
HCW226	F	3	yes	pre Omicron	25	preOm+vacc
HCW228	M	3	yes	pre Omicron	20	preOm+vacc

HCW232	F	3	yes	pre Omicron	25	preOm+vacc
HCW234	M	3	yes	pre Omicron	19	preOm+vacc
HCW236	F	3	yes	pre Omicron	27	preOm+vacc
HCW237	F	3	yes	pre Omicron	20	preOm+vacc
HCW238	M	3	yes	pre Omicron	26	preOm+vacc
HCW240	F	3	yes	pre Omicron	26	preOm+vacc
HCW242	F	3	yes	pre Omicron	25	preOm+vacc
VC338	F	4	no	/	13	Wu/BA.1biv
VC343	F	4	no	/	13	Wu/BA.1biv
VC344	M	4	no	/	12	Wu/BA.1biv
VC345	M	4	no	/	13	Wu/BA.1biv
VC346	M	4	no	/	13	Wu/BA.1biv
VC348	M	4	no	/	13	Wu/BA.1biv
VC349	F	4	no	/	19	Wu/BA.1biv
VC339	F	4	yes	Omicron BA.1/BA.2	13	Om.BT+biv
VC340	F	4	yes	Omicron BA.1/BA.2	13	Om.BT+biv
VC341	F	4	yes	Omicron BA.1/BA.2	13	Om.BT+biv
VC342	F	4	yes	Omicron BA.1/BA.2	12	Om.BT+biv
VC347	M	4	yes	Omicron BA.1/BA.2	13	Om.BT+biv

*Donor 31H received the Janssen COVID-19 vaccination as primary vaccine series.

1123

1124 **Supplementary Table 6. Kidney transplant recipients' and healthcare workers'**
1125 **demographics.**

Donor ID	Gender	No. of immunosuppressive drugs*	Vaccine doses	COVID diagnosis	SARS-CoV-2 variant	D sample-vaccine (days)	Cohort
KTR-004	M	2	4	no	/	83	KTR Wu_4vacc
KTR-007	M	3	4	no	/	140	KTR Wu_4vacc
KTR-009	M	2	4	no	/	46	KTR Wu_4vacc
KTR-010	F	3	4	no	/	51	KTR Wu_4vacc
KTR-011	M	2	4	no	/	80	KTR Wu_4vacc
KTR-013	F	1	4	no	/	92	KTR Wu_4vacc
KTR-026	M	2	4	no	/	63	KTR Wu_4vacc
KTR-027	F	3	4	no	/	35	KTR Wu_4vacc
KTR-030	M	2	4	no	/	71	KTR Wu_4vacc
KTR-039	M	2	4	no	/	77	KTR Wu_4vacc
KTR-042	M	3	4	no	/	40	KTR Wu_4vacc
KTR-047	M	2	4	no	/	76	KTR Wu_4vacc
KTR-050	M	2	4	no	/	84	KTR Wu_4vacc
KTR-054	M	2	4	no	/	18	KTR Wu_4vacc
KTR-056	M	2	4	no	/	70	KTR Wu_4vacc
KTR-059	M	2	4	no	/	78	KTR Wu_4vacc
KTR-060	M	2	4	no	/	71	KTR Wu_4vacc
KTR-061	M	2	4	no	/	54	KTR Wu_4vacc
KTR-071	F	3	4	no	/	35	KTR Wu_4vacc
KTR-083	M	3	4	no	/	82	KTR Wu_4vacc
KTR-085	F	2	4	no	/	71	KTR Wu_4vacc
KTR-094	M	2	4	no	/	41	KTR Wu_4vacc
KTR-095	M	3	4	no	/	74	KTR Wu_4vacc
KTR-096	M	2	4	no	/	43	KTR Wu_4vacc
KTR-101	M	2	4	no	/	72	KTR Wu_4vacc
KTR-102	M	3	4	no	/	133	KTR Wu_4vacc
KTR-017	F	2	4	yes	pre Omicron	58	KTR preOm+Wu_4vacc
KTR-021	M	2	4	yes	pre Omicron	84	KTR preOm+Wu_4vacc
KTR-031	F	2	4	yes	pre Omicron	59	KTR preOm+Wu_4vacc
KTR-084	F	3	4	yes	pre Omicron	65	KTR preOm+Wu_4vacc
KTR-099	M	2	4	yes	pre Omicron	93	KTR preOm+Wu_4vacc
HCW-001	M	/	3	no	/	90	HCW Wu_3vacc
HCW-002	F	/	3	no	/	78	HCW Wu_3vacc
HCW-003	F	/	3	no	/	76	HCW Wu_3vacc
HCW-004	M	/	3	no	/	90	HCW Wu_3vacc
HCW-005	F	/	3	no	/	83	HCW Wu_3vacc
HCW-008	F	/	3	no	/	86	HCW Wu_3vacc
HCW-009	F	/	3	no	/	81	HCW Wu_3vacc
HCW-011	M	/	3	no	/	93	HCW Wu_3vacc
HCW-012	F	/	3	no	/	94	HCW Wu_3vacc
HCW-013	F	/	3	no	/	55	HCW Wu_3vacc
HCW-016	F	/	3	no	/	6	HCW Wu_3vacc
HCW-017	F	/	3	no	/	50	HCW Wu_3vacc
HCW-018	M	/	3	no	/	110	HCW Wu_3vacc
HCW-019	F	/	3	no	/	29	HCW Wu_3vacc
HCW-020	F	/	3	no	/	90	HCW Wu_3vacc
HCW-021	M	/	3	no	/	28	HCW Wu_3vacc
HCW-022	F	/	3	no	/	28	HCW Wu_3vacc
HCW-023	F	/	3	no	/	22	HCW Wu_3vacc
HCW-024	M	/	3	no	/	35	HCW Wu_3vacc
HCW-025	F	/	3	no	/	94	HCW Wu_3vacc
HCW-026	F	/	3	no	/	28	HCW Wu_3vacc
HCW-027	F	/	3	no	/	38	HCW Wu_3vacc
HCW-028	F	/	3	no	/	29	HCW Wu_3vacc

HCW-031	F	/	3	no	/	35	HCW Wu_3vacc
HCW-033	F	/	3	no	/	31	HCW Wu_3vacc
HCW-037	F	/	3	no	/	45	HCW Wu_3vacc
HCW-038	F	/	3	no	/	61	HCW Wu_3vacc
HCW-039	F	/	3	no	/	23	HCW Wu_3vacc
HCW-010	F	/	3	yes	pre Omicron	69	HCW preOm+Wu_3vacc
HCW-014	F	/	3	yes	pre Omicron	89	HCW preOm+Wu_3vacc
HCW-015	F	/	3	yes	pre Omicron	86	HCW preOm+Wu_3vacc
HCW-029	F	/	3	yes	pre Omicron	77	HCW preOm+Wu_3vacc
HCW-030	F	/	3	yes	pre Omicron	35	HCW preOm+Wu_3vacc
HCW-034	F	/	3	yes	pre Omicron	28	HCW preOm+Wu_3vacc
HCW-036	F	/	3	yes	pre Omicron	34	HCW preOm+Wu_3vacc

*any of the following: cyclosporin, tacrolimus, MMF/MPA, azathioprine, everolimus/sirolimus, belatacept or glucocorticoids

References

1. Cao, Y. *et al.* Imprinted SARS-CoV-2 humoral immunity induces convergent Omicron RBD evolution. *Nature* (2022) doi:10.1038/s41586-022-05644-7.
2. Viana, R. *et al.* Rapid epidemic expansion of the SARS-CoV-2 Omicron variant in southern Africa. *Nature* (2022) doi:10.1038/d41586-021-03832-5.
3. Bowen, J. E. *et al.* Omicron spike function and neutralizing activity elicited by a comprehensive panel of vaccines. *Science* eabq0203 (2022).
4. Cameroni, E. *et al.* Broadly neutralizing antibodies overcome SARS-CoV-2 Omicron antigenic shift. *Nature* **602**, 664–670 (2022).
5. McCallum, M. *et al.* Structural basis of SARS-CoV-2 Omicron immune evasion and receptor engagement. *Science* eabn8652 (2022).
6. Meng, B. *et al.* Altered TMPRSS2 usage by SARS-CoV-2 Omicron impacts infectivity and fusogenicity. *Nature* **603**, 706–714 (2022).
7. Peacock, T. P. *et al.* The altered entry pathway and antigenic distance of the SARS-CoV-2 Omicron variant map to separate domains of spike protein. *bioRxiv* 2021.12.31.474653 (2022) doi:10.1101/2021.12.31.474653.
8. Willett, B. J. *et al.* SARS-CoV-2 Omicron is an immune escape variant with an altered cell entry pathway. *Nat Microbiol* **7**, 1161–1179 (2022).
9. Planas, D. *et al.* Considerable escape of SARS-CoV-2 Omicron to antibody neutralization. *Nature* (2021) doi:10.1038/d41586-021-03827-2.
10. Liu, L. *et al.* Striking antibody evasion manifested by the Omicron variant of SARS-CoV-2. *Nature* (2021) doi:10.1038/d41586-021-03826-3.
11. Cao, Y. *et al.* Omicron escapes the majority of existing SARS-CoV-2 neutralizing antibodies. *Nature* (2021) doi:10.1038/d41586-021-03796-6.
12. Mlcochova, P. *et al.* SARS-CoV-2 B.1.617.2 Delta variant replication and immune evasion. *Nature* (2021) doi:10.1038/s41586-021-03944-y.
13. Carreño, J. M. *et al.* Activity of convalescent and vaccine serum against SARS-CoV-2 Omicron. *Nature* **602**, 682–688 (2022).
14. Akerman, A. *et al.* Emergence and antibody evasion of BQ and BA.2.75 SARS-CoV-2 sublineages in the face of maturing antibody breadth at the population level. *bioRxiv* (2022) doi:10.1101/2022.12.06.22283000.
15. Aggarwal, A. *et al.* SARS-CoV-2 Omicron BA.5: Evolving tropism and evasion of potent humoral responses and resistance to clinical immunotherapeutics relative to viral variants of concern. *EBioMedicine* **84**, 104270 (2022).
16. Gregory, D. A. *et al.* Genetic diversity and evolutionary convergence of cryptic SARS- CoV-2 lineages detected via wastewater sequencing. *PLOS Pathogens* vol. 18 e1010636 at https://doi.org/10.1371/journal.ppat.1010636 (2022).
17. Walls, A. C. *et al.* Structure, Function, and Antigenicity of the SARS-CoV-2 Spike Glycoprotein. *Cell* **181**, 281-292.e6 (2020).
18. Wrapp, D. *et al.* Cryo-EM structure of the 2019-nCoV spike in the prefusion conformation. *Science* **367**, 1260–1263 (2020).
19. Hoffmann, M. *et al.* SARS-CoV-2 Cell Entry Depends on ACE2 and TMPRSS2 and Is Blocked by a Clinically Proven Protease Inhibitor. *Cell* **181**, 271-280.e8 (2020).

1174 20. Letko, M., Marzi, A. & Munster, V. Functional assessment of cell entry and receptor usage
1175 for SARS-CoV-2 and other lineage B betacoronaviruses. *Nature Microbiology* (2020)
1176 doi:10.1038/s41564-020-0688-y.
1177 21. Arunachalam, P. S. *et al.* Durable protection against the SARS-CoV-2 Omicron variant is
1178 induced by an adjuvanted subunit vaccine. *Sci. Transl. Med.* **14**, eabq4130 (2022).
1179 22. Arunachalam, P. S. *et al.* Adjuvanting a subunit COVID-19 vaccine to induce protective
1180 immunity. *Nature* (2021) doi:10.1038/s41586-021-03530-2.
1181 23. Piccoli, L. *et al.* Mapping Neutralizing and Immunodominant Sites on the SARS-CoV-2
1182 Spike Receptor-Binding Domain by Structure-Guided High-Resolution Serology. *Cell* **183**,
1183 1024-1042.e21 (2020).
1184 24. McCallum, M. *et al.* N-terminal domain antigenic mapping reveals a site of vulnerability for
1185 SARS-CoV-2. *Cell* (2021) doi:10.1016/j.cell.2021.03.028.
1186 25. Cromer, D. *et al.* Neutralising antibody titres as predictors of protection against SARS-CoV-
1187 2 variants and the impact of boosting: a meta-analysis. *Lancet Microbe* **3**, e52–e61 (2022).
1188 26. Goldblatt, D., Alter, G., Crotty, S. & Plotkin, S. A. Correlates of protection against SARS-
1189 CoV-2 infection and COVID-19 disease. *Immunol. Rev.* **310**, 6–26 (2022).
1190 27. Khoury, D. S. *et al.* Neutralizing antibody levels are highly predictive of immune protection
1191 from symptomatic SARS-CoV-2 infection. *Nat. Med.* **27**, 1205–1211 (2021).
1192 28. McMahan, K. *et al.* Correlates of protection against SARS-CoV-2 in rhesus macaques.
1193 *Nature* **590**, 630–634 (2021).
1194 29. Corbett, K. S. *et al.* Immune correlates of protection by mRNA-1273 vaccine against SARS-
1195 CoV-2 in nonhuman primates. *Science* (2021) doi:10.1126/science.abj0299.
1196 30. Cho, A. *et al.* Anti-SARS-CoV-2 receptor binding domain antibody evolution after mRNA
1197 vaccination. *Nature* (2021) doi:10.1038/s41586-021-04060-7.
1198 31. Robbiani, D. F. *et al.* Convergent antibody responses to SARS-CoV-2 in convalescent
1199 individuals. *Nature* (2020) doi:10.1038/s41586-020-2456-9.
1200 32. Barnes, C. O. *et al.* SARS-CoV-2 neutralizing antibody structures inform therapeutic
1201 strategies. *Nature* **588**, 682–687 (2020).
1202 33. Amanat, F. *et al.* Murine monoclonal antibodies against the receptor binding domain of
1203 SARS-CoV-2 neutralize authentic wild-type SARS-CoV-2 as well as B.1.1.7 and B.1.351
1204 viruses and protect in vivo in a mouse model in a neutralization-dependent manner. *MBio*
1205 **12**, e0100221 (2021).
1206 34. Hastie, K. M. *et al.* Defining variant-resistant epitopes targeted by SARS-CoV-2 antibodies:
1207 A global consortium study. *Science* **374**, 472–478 (2021).
1208 35. Starr, T. N. *et al.* Deep mutational scans for ACE2 binding, RBD expression, and antibody
1209 escape in the SARS-CoV-2 Omicron BA.1 and BA.2 receptor-binding domains. *PLoS*
1210 *Pathog.* **18**, e1010951 (2022).
1211 36. Starr, T. N. *et al.* Deep Mutational Scanning of SARS-CoV-2 Receptor Binding Domain
1212 Reveals Constraints on Folding and ACE2 Binding. *Cell* **182**, 1295-1310.e20 (2020).
1213 37. McCallum, M. *et al.* Molecular basis of immune evasion by the Delta and Kappa SARS-
1214 CoV-2 variants. *Science* eabl8506 (2021).
1215 38. Kodaka, M. *et al.* A new cell-based assay to evaluate myogenesis in mouse myoblast
1216 C2C12 cells. *Exp. Cell Res.* **336**, 171–181 (2015).

1217 39. Meng, B. *et al.* SARS-CoV-2 spike N-terminal domain modulates TMPRSS2-dependent
1218 viral entry and fusogenicity. *Cell Rep.* **40**, 111220 (2022).
1219 40. Lan, J. *et al.* Structure of the SARS-CoV-2 spike receptor-binding domain bound to the
1220 ACE2 receptor. *Nature* (2020) doi:10.1038/s41586-020-2180-5.
1221 41. Wang, Q. *et al.* Alarming antibody evasion properties of rising SARS-CoV-2 BQ and XBB
1222 subvariants. *Cell* (2022) doi:10.1016/j.cell.2022.12.018.
1223 42. Pinto, D. *et al.* Cross-neutralization of SARS-CoV-2 by a human monoclonal SARS-CoV
1224 antibody. *Nature* **583**, 290–295 (2020).
1225 43. Park, Y.-J. *et al.* Imprinted antibody responses against SARS-CoV-2 Omicron sublineages.
1226 *Science* eadc9127 (2022).
1227 44. Stalls, V. *et al.* Cryo-EM structures of SARS-CoV-2 Omicron BA.2 spike. *Cell Rep.* **39**,
1228 111009 (2022).
1229 45. Cao, Y. *et al.* BA.2.12.1, BA.4 and BA.5 escape antibodies elicited by Omicron infection.
1230 *Nature* **608**, 593–602 (2022).
1231 46. Planas, D. *et al.* Resistance of Omicron subvariants BA.2.75.2, BA.4.6 and BQ.1.1 to
1232 neutralizing antibodies. *bioRxivorg* (2022) doi:10.1101/2022.11.17.516888.
1233 47. Yue, C. *et al.* Enhanced transmissibility of XBB.1.5 is contributed by both strong ACE2
1234 binding and antibody evasion. *bioRxiv* (2023) doi:10.1101/2023.01.03.522427.
1235 48. Starr, T. N. *et al.* SARS-CoV-2 RBD antibodies that maximize breadth and resistance to
1236 escape. *Nature* (2021) doi:10.1038/s41586-021-03807-6.
1237 49. Driouich, J.-S., Bernardin, O., Touret, F., de Lamballerie, X. & Nougairède, A. In vivo
1238 activity of Sotrovimab against BQ.1.1 Omicron sublineage. *bioRxiv* (2023)
1239 doi:10.1101/2023.01.04.522629.
1240 50. Carreño, J. M. *et al.* Evidence for retained spike-binding and neutralizing activity against
1241 emerging SARS-CoV-2 variants in serum of COVID-19 mRNA vaccine recipients.
1242 *EBioMedicine* **73**, 103626 (2021).
1243 51. Quandt, J. *et al.* Omicron BA.1 breakthrough infection drives cross-variant neutralization
1244 and memory B cell formation against conserved epitopes. *Sci. Immunol.* **7**, eabq2427
1245 (2022).
1246 52. Muecksch, F. *et al.* Increased memory B cell potency and breadth after a SARS-CoV-2
1247 mRNA boost. *Nature* **607**, 128–134 (2022).
1248 53. Wang, Z. *et al.* Naturally enhanced neutralizing breadth against SARS-CoV-2 one year
1249 after infection. *Nature* **595**, 426–431 (2021).
1250 54. Muecksch, F. *et al.* Affinity maturation of SARS-CoV-2 neutralizing antibodies confers
1251 potency, breadth, and resilience to viral escape mutations. *Immunity* **54**, 1853-1868.e7
1252 (2021).
1253 55. Marzi, R. *et al.* Maturation of SARS-CoV-2 Spike-specific memory B cells drives resilience
1254 to viral escape. *iScience* **26**, 105726 (2023).
1255 56. Gaebler, C. *et al.* Evolution of antibody immunity to SARS-CoV-2. *Nature* **591**, 639–644
1256 (2021).
1257 57. Zhang, Z. *et al.* Humoral and cellular immune memory to four COVID-19 vaccines. *Cell*
1258 **185**, 2434-2451.e17 (2022).
1259 58. Turner, J. S. *et al.* SARS-CoV-2 mRNA vaccines induce persistent human germinal centre
1260 responses. *Nature* **596**, 109–113 (2021).

1261 59. Dan, J. M. *et al.* Immunological memory to SARS-CoV-2 assessed for up to 8 months after
1262 infection. *Science* **371**, eabf4063 (2021).
1263 60. Markov, P. V., Katzourakis, A. & Stilianakis, N. I. Antigenic evolution will lead to new SARS-
1264 CoV-2 variants with unpredictable severity. *Nat. Rev. Microbiol.* **20**, 251–252 (2022).
1265 61. Kemp, S. A. *et al.* SARS-CoV-2 evolution during treatment of chronic infection. *Nature* **592**,
1266 277–282 (2021).
1267 62. Sette, A. & Crotty, S. Adaptive immunity to SARS-CoV-2 and COVID-19. *Cell* **184**, 861–880
1268 (2021).
1269 63. Zhang, A. *et al.* Beyond neutralization: Fc-dependent antibody effector functions in SARS-
1270 CoV-2 infection. *Nat. Rev. Immunol.* (2022) doi:10.1038/s41577-022-00813-1.
1271 64. Kaplonek, P. *et al.* mRNA-1273 and BNT162b2 COVID-19 vaccines elicit antibodies with
1272 differences in Fc-mediated effector functions. *Sci. Transl. Med.* **14**, eabm2311 (2022).
1273 65. Kaplonek, P. *et al.* mRNA-1273 vaccine-induced antibodies maintain Fc effector functions
1274 across SARS-CoV-2 variants of concern. *Immunity* **55**, 355-365.e4 (2022).
1275 66. Feng, S. *et al.* Correlates of protection against symptomatic and asymptomatic SARS-CoV-
1276 2 infection. *Nat. Med.* **27**, 2032–2040 (2021).
1277 67. Case, J. B. *et al.* Resilience of S309 and AZD7442 monoclonal antibody treatments against
1278 infection by SARS-CoV-2 Omicron lineage strains. *Nat. Commun.* **13**, 3824 (2022).
1279 68. Zheng, B. *et al.* Comparative effectiveness of sotrovimab and molnupiravir for prevention of
1280 severe covid-19 outcomes in patients in the community: observational cohort study with the
1281 OpenSAFELY platform. *BMJ* **379**, e071932 (2022).
1282 69. Cheng, M. M. *et al.* Real-world effectiveness of sotrovimab for the early treatment of
1283 COVID-19 during SARS-CoV-2 Delta and Omicron waves in the USA. *Infect. Dis. Ther.*
1284 (2023) doi:10.1007/s40121-022-00755-0.
1285 70. Martin-Blondel, G. *et al.* Sotrovimab to prevent severe COVID-19 in high-risk patients
1286 infected with Omicron BA.2. *J. Infect.* **85**, e104–e108 (2022).
1287 71. Harman, K. *et al.* Comparison of the risk of hospitalisation among BA.1 and BA.2 COVID-
1288 19 cases treated with Sotrovimab in the community in England. *bioRxiv* (2022)
1289 doi:10.1101/2022.10.21.22281171.
1290 72. Young-Xu, Y. *et al.* Effectiveness of sotrovimab in preventing COVID-19-related
1291 hospitalizations or deaths among U.s. veterans. *bioRxiv* (2022)
1292 doi:10.1101/2022.12.30.22284063.
1293 73. Bartsch, Y. C. *et al.* Omicron variant Spike-specific antibody binding and Fc activity are
1294 preserved in recipients of mRNA or inactivated COVID-19 vaccines. *Sci. Transl. Med.* **14**,
1295 eabn9243 (2022).
1296 74. Richardson, S. I. *et al.* Antibody-dependent cellular cytotoxicity against SARS-CoV-2
1297 Omicron sub-lineages is reduced in convalescent sera regardless of infecting variant. *Cell*
1298 *Rep. Med.* 100910 (2022).
1299 75. Mackin, S. R. *et al.* Fcγ receptor-dependent antibody effector functions are required for
1300 vaccine protection against infection by antigenic variants of SARS-CoV-2. *bioRxivorg*
1301 (2022) doi:10.1101/2022.11.27.518117.
1302 76. Bergwerk, M. *et al.* Covid-19 breakthrough infections in vaccinated health care workers. *N.*
1303 *Engl. J. Med.* **385**, 1474–1484 (2021).

77. Francis, T. On the doctrine of original antigenic sin. *Proc Am Philos Soc* **104**, 572–578 (1960).
78. Corti, D. *et al.* A neutralizing antibody selected from plasma cells that binds to group 1 and group 2 influenza A hemagglutinins. *Science* **333**, 850–856 (2011).
79. Wrammert, J. *et al.* Broadly cross-reactive antibodies dominate the human B cell response against 2009 pandemic H1N1 influenza virus infection. *J. Exp. Med.* **208**, 181–193 (2011).
80. Cheung, C. S.-F. *et al.* Identification and structure of a multidonor class of head-directed influenza-neutralizing antibodies reveal the mechanism for its recurrent elicitation. *Cell Rep.* **32**, 108088 (2020).
81. Nachbagauer, R. *et al.* A chimeric hemagglutinin-based universal influenza virus vaccine approach induces broad and long-lasting immunity in a randomized, placebo-controlled phase I trial. *Nat. Med.* **27**, 106–114 (2021).
82. Walls, A. C. *et al.* Elicitation of broadly protective sarbecovirus immunity by receptor-binding domain nanoparticle vaccines. *Cell* (2021) doi:10.1016/j.cell.2021.09.015.
83. Walls, A. C. *et al.* Elicitation of Potent Neutralizing Antibody Responses by Designed Protein Nanoparticle Vaccines for SARS-CoV-2. *Cell* **183**, 1367-1382.e17 (2020).
84. Martinez, D. R. *et al.* Chimeric spike mRNA vaccines protect against Sarbecovirus challenge in mice. *Science* (2021) doi:10.1126/science.abi4506.
85. Cohen, A. A. *et al.* Mosaic RBD nanoparticles protect against challenge by diverse sarbecoviruses in animal models. *Science* **377**, eabq0839 (2022).
86. Cohen, A. A. *et al.* Mosaic nanoparticles elicit cross-reactive immune responses to zoonotic coronaviruses in mice. *Science* **371**, 735–741 (2021).
87. Li, D. *et al.* Breadth of SARS-CoV-2 neutralization and protection induced by a nanoparticle vaccine. *Nat. Commun.* **13**, 6309 (2022).
88. González-Domínguez, I. *et al.* Trivalent NDV-HXP-S vaccine protects against phylogenetically distant SARS-CoV-2 variants of concern in mice. *Microbiol. Spectr.* **10**, e0153822 (2022).
89. Sano, K. *et al.* SARS-CoV-2 vaccination induces mucosal antibody responses in previously infected individuals. *Nat. Commun.* **13**, 5135 (2022).
90. Mao, T. *et al.* Unadjuvanted intranasal spike vaccine elicits protective mucosal immunity against sarbecoviruses. *Science* **378**, eabo2523 (2022).
91. Hassan, A. O. *et al.* An intranasal vaccine durably protects against SARS-CoV-2 variants in mice. *Cell Rep.* **36**, 109452 (2021).